nature chemical biology

Article

https://doi.org/10.1038/s41589-025-02134-5

Molecular insight into 5′ RNA capping with Np$_n$Ns by bacterial RNA polymerase

Received: 7 November 2024

Accepted: 18 December 2025

Valentina M. Serianni[1,2,3], Jana Škerlová[1,3], Anna Knopp Dubánková[1], Anton Škríba[1], Hana Šváchová[1], Tereza Vučková[1], Anatolij Filimoněnko[1], Milan Fábry[1], Pavlína Řezáčová[1], Tomáš Kouba[1] & Hana Cahova[1]

RNA capped with dinucleoside polyphosphates has been discovered in bacteria and eukaryotes only recently. The likely mechanism of this specific capping involves direct incorporation of dinucleoside polyphosphates by RNA polymerase as noncanonical initiating nucleotides. However, how these compounds bind into the active site of RNA polymerase during transcription initiation is unknown. Here, we explored transcription initiation in vitro, using a series of DNA templates in combination with dinucleoside polyphosphates and model RNA polymerase from *Thermus thermophilus*. We observed that the transcription start site can vary on the basis of the compatibility of the specific template and dinucleoside polyphosphate. Cryo-electron microscopy structures of transcription initiation complexes with dinucleoside polyphosphates revealed that both nucleobase moieties can pair with the DNA template. The first encoded nucleotide pairs in a canonical Watson–Crick manner, whereas the second nucleobase pairs noncanonically in a reverse Watson–Crick manner. Our work provides a structural explanation of how dinucleoside polyphosphates initiate RNA transcription.

RNA modifications have important roles in the life of RNA, including its stabilization, localization and specific recognition of its interacting partners. More than 170 RNA modifications are known[1] in all types of organisms. Their roles are understood and well described in the most abundant types of RNA such as transfer RNA and ribosomal RNA. However, their function in other types of RNA, like mRNA or long noncoding RNA, is still under investigation. Some of the best-described RNA modifications are canonical 5′ m^{7}G caps, which are known to have an important role in eukaryotic mRNAs. The discovery of 5′ noncanonical capping of RNA, namely the capping of RNA with nicotinamide adenine dinucleotide (NAD)[2–5] and coenzyme A (CoA)[6], triggered a search for other alternative RNA caps. Lately, flavin adenine dinucleotide (FAD)[7,8], sugar conjugate[9] and dinucleoside polyphosphate (Np$_n$Ns)[10–12] RNA caps have been discovered in a variety of organisms[13].

The most widely accepted hypothesis concerning the biosynthesis of noncanonically capped RNA is that RNA polymerases (RNAPs) directly use these molecules as noncanonical initiating nucleotides (NCINs). This is analogous to noncanonical transcription initiation by 5′-end hydroxyl dinucleotide primers[14,15], which are used instead of regular nucleoside triphosphates (NTPs). The ability of bacterial or bacteriophage RNAP to initiate transcription with NAD, CoA or FAD cofactor molecules was first described in vitro[16,17]. Later on, cofactor incorporation by bacterial and eukaryotic RNAP II was confirmed in vivo, as well[18]. X-ray structures of *Thermus thermophilus* (*Tt*) RNAP visualized these cofactors as NCINs[18].

Various types of Np$_n$Ns serving as RNA caps have been detected in *Escherichia coli* by using liquid chromatography–mass spectrometry (LC–MS) analysis[11]. We and others have demonstrated that Np$_n$Ns can be incorporated into RNA directly by bacteriophage and bacterial RNAPs as NCINs[11,19] in a similar manner as cofactors.

In our previous study, we focused on the direct incorporation of Np$_n$Ns by RNAP during the initiation phase of transcription[20]. We observed that the addition of Np$_n$Ns, such as Ap$_3$G, into an in vitro transcription (IVT) reaction with T7 RNAP led to a several times greater

---

[1]Institute of Organic Chemistry and Biochemistry of the CAS, Flemingovo náměstí 2, Prague, Czechia. [2]Charles University, Faculty of Science, Department of Cell Biology, Viničná 7, Prague, Czechia. [3]These authors contributed equally: Valentina M. Serianni, Jana Škerlová. e-mail: tomas.kouba@uochb.cas.cz; hana.cahova@uochb.cas.cz

production of 2-mer or 3-mer RNAs. It is important to note that because Np$_n$Ns are linked 5′ to 5′ (Fig. 1a and Extended Data Fig. 1), they have two free 3′ hydroxyl groups and can be incorporated into a nascent RNA chain in two alternative orientations. Molecular dynamics simulations predicted that both nucleosides from the Ap$_3$G NCIN pair with the template DNA strand. Whereas G paired in the RNAP *i* site with the template transcription start site (TSS) +1C in a Watson–Crick (WC) manner, A paired in the *i* − 1 site with the template −1T in a noncanonical manner. In comparison, the 5′-end hydroxyl dinucleotide primers, where the direction of incorporation of the dinucleotides is governed by the canonical 5′-to-3′ linkage, pair in the regular WC manner in both *i* and *i* − 1 sites[15].

To further investigate the details of the initiation phase of transcription with NCINs in bacteria, we focused on *Tt* RNAP as a robust structural model of bacterial transcription and on purine-containing Np$_n$Ns, which are the most studied examples of Np$_n$Ns in bacteria[21–23]. Moreover, *Tt* σ^A belongs to the same family of sigma factors[24] as housekeeping *E. coli* σ^{70}, which has been reported to initiate transcription primarily with ATP or GTP[25]. We designed experiments where various Np$_n$Ns (Ap$_{3\text{-}4}$A, Ap$_{3\text{-}4}$G and Gp$_{3\text{-}4}$G) were probed as NCINs by IVT assays with templates having combinations of T and/or C at positions −1 and +1 of the template strand with respect to the TSS. Following on these experiments, we visualized, using cryogenic electron microscopy (cryo-EM), a set of *Tt* RNAP transcription initiation complexes with various Ap$_n$Ns bound as NCINs to templates in the RNAP active site (AS). The structural analysis confirmed that both nucleosides of Ap$_n$Ns can base pair with the template DNA strand and provided a structural basis for understanding their role as NCINs.

Results

Two possible ways of transcription initiation with Np$_n$Ns

To explore the role of Np$_n$Ns in the transcription initiation process, we designed a series of templates with artificial transcription bubbles for use in an IVT assay using the *Tt* RNAP-σ^A holoenzyme[26]. The templates were designed on the basis of previous work[27,28] (Fig. 1, Extended Data Table 1, Supplementary Table 1 and Supplementary Fig. 1), having combinations of C and/or T at positions −1 and +1 of the template strand with respect to the TSS. We then performed radioactively labeled IVT reactions using these templates with four regular NTPs in combination with Np$_n$Ns (Ap$_{3\text{-}4}$A, Ap$_{3\text{-}4}$G and Gp$_{3\text{-}4}$G; Fig. 1b,c). We prepared control experiments where the concentration of Np$_n$Ns was replaced by the two respective NTPs (ATP or GTP). Each control contained the same total final concentration of initiating nucleotides (Supplementary Table 2).

The control reactions using the template TC and regular NTPs resulted in the production of the expected 15-mer product ((+1) TSS-RNA), initiating at the putative +1C TSS (Fig. 1c,d). We also observed formation of a 1-nt-longer product potentially starting at the −1T TSS ((−1)TSS-RNA) and other shorter aberrant products (Fig. 1c,d), which might be abortive products, as previously reported for IVTs using *E. coli* RNAP[29,30]. When we used the template TC and added Np$_n$Ns into the IVT mixture, we observed the formation of capped RNA of two different lengths, depending on the type of Np$_n$N (Fig. 1c,d). The addition of Ap$_{3\text{-}4}$G and Gp$_{3\text{-}4}$G in the reaction mixture led to the formation of a dominant RNA product migrating slower in PAGE than the control RNA without Np$_n$Ns (15-mer). The size of this RNA corresponds to a capped 15-mer transcription product starting with the G nucleoside of Np$_n$G at position +1C of the template (cap(+1)TSS-RNA). This potentially allows the A nucleoside of Ap$_{3\text{-}4}$G to interact with the −1T base of the template (Fig. 1b). In experiments with added Ap$_{3\text{-}4}$G, we also observed traces of a capped 16-mer RNA product (cap(−1)TSS-RNA). This suggests that Ap$_{3\text{-}4}$G can initiate transcription with the A moiety at the template −1T position. However, this would require a shift of the template strand by one nucleotide with respect to the RNAP AS for the −1 template position to serve as the TSS. Variability in TSS selection has been already described and involves DNA scrunching and antiscrunching[31–33]. Lastly, when we added Ap$_{3\text{-}4}$A to the IVT reactions, we observed the formation of the capped 16-mer transcription product (cap(−1)TSS-RNA; Fig. 1d). This suggests that initiation by Ap$_{3\text{-}4}$A leads to the production of capped RNA encoded from the −1T position rather than from the putative +1C position of the DNA template.

To confirm the results of the IVT PAGE experiments and, thus, verify that we observed Np$_n$N-capped RNA products initiating at the +1 and −1 template positions as the TSSs, we established a very sensitive LC–MS method capable of detecting the full-length products of IVT with *Tt* RNAP. We were able to identify all expected IVT products, encoded from both the +1 TSS and the −1 TSS (Fig. 1c), in the reaction mixtures containing Np$_n$Ns or in the control mixtures (Supplementary Table 3 and Extended Data Fig. 2). Surprisingly, we also detected unexpected products with an extra C added at the 3′ end (Supplementary Table 3, Extended Data Fig. 2 and Supplementary Fig. 2), indicating that, for example, the IVT PAGE band corresponding to a 16-mer (Fig. 1d) contains, in addition to the (−1)TSS-RNA, a (+1)TSS-RNA with an extra 3′ C. Similar nontemplated addition of C at the 3′ end of RNA has been already reported for mitochondrial RNAP of the protist *Physarum polycephalum*[34,35].

To understand whether capped RNA is also formed by *Tt* RNAP in the context of native-like DNA promoter, we developed another transcription assay using a circular supercoiled plasmid (plasmid TC)[36] Supplementary Table 1) containing a fully complementary promoter with the −35 and −10 elements used in this study and with a T at the −1 position and a C at the +1 position, resembling the TC template. Using this assay, we observed the formation of all Np$_n$N-capped RNAs through PAGE and LC–MS analysis combined with RNase A treatment (Extended Data Fig. 3 and Supplementary Table 4).

Furthermore, we performed the same IVT and LC–MS experiments as for template TC also on additional templates containing combinations of C and/or T at positions −1 and +1 of the template strand (templates gTT and CT) (Extended Data Table 1, Extended Data Figs. 4–7 and Supplementary Tables 5 and 6). Indeed, we confirmed that the *Tt* RNAP holoenzyme in combination with the DNA templates used in this study allow the Np$_n$Ns to initiate transcription from both the +1 and −1 template positions as TSSs. Additionally, when using NAD as NCIN in the IVT, we confirmed that it has a much lower incorporation efficiency[19] than NTPs and Np$_n$Ns (Supplementary Fig. 3).

Structural insights into transcription initiation by Np$_n$Ns

During transcription initiation, RNAP catalyzes the synthesis of the first phosphodiester bond between the initiating nucleotide bound in the *i* site (+1 with respect to the canonical TSS of the template) and the extending nucleotide bound in the *i* + 1 site (+2 with respect to the canonical TSS of the template) of the catalytic site. Previous structural studies defined NCINs to be able to react de novo in the catalytic site of bacterial RNAP[18]. However, the binding of NCINs into the *i* site and the *i* − 1 site (−1 with respect to the canonical TSS of the template) to react with an extending nucleotide was never captured. This is because the NCINs were allowed to react with the extending nucleotide and the AS was visualized in a posttranslocated state. Here, we aimed to visualize the state just before the very first step of the initial nucleotidyl transfer, where NCINs align to react with the first extending nucleotide (Supplementary Fig. 4), but before the reaction occurs—in the precatalytic state. For this purpose, we reconstituted an artificial *Tt* holoenzyme complex with an opened transcription bubble with defined mixtures of substrates and nonhydrolyzable analogs.

We first visualized, using cryo-EM, the canonical de novo transcription initiation complex with template TC together with GTP and the nonhydrolyzable CTP analog cytidine-5′-[(α,β)-methyleno]triphosphate (CMPcPP). The cryo-EM analysis (Supplementary Figs. 5 and 6 and Supplementary Tables 7 and 8) revealed two relevant structures, one with an unoccupied AS, hereafter referred to as TC-empty, and one with the AS occupied by GTP and CMPcPP, hereafter referred to as TC-GTP.

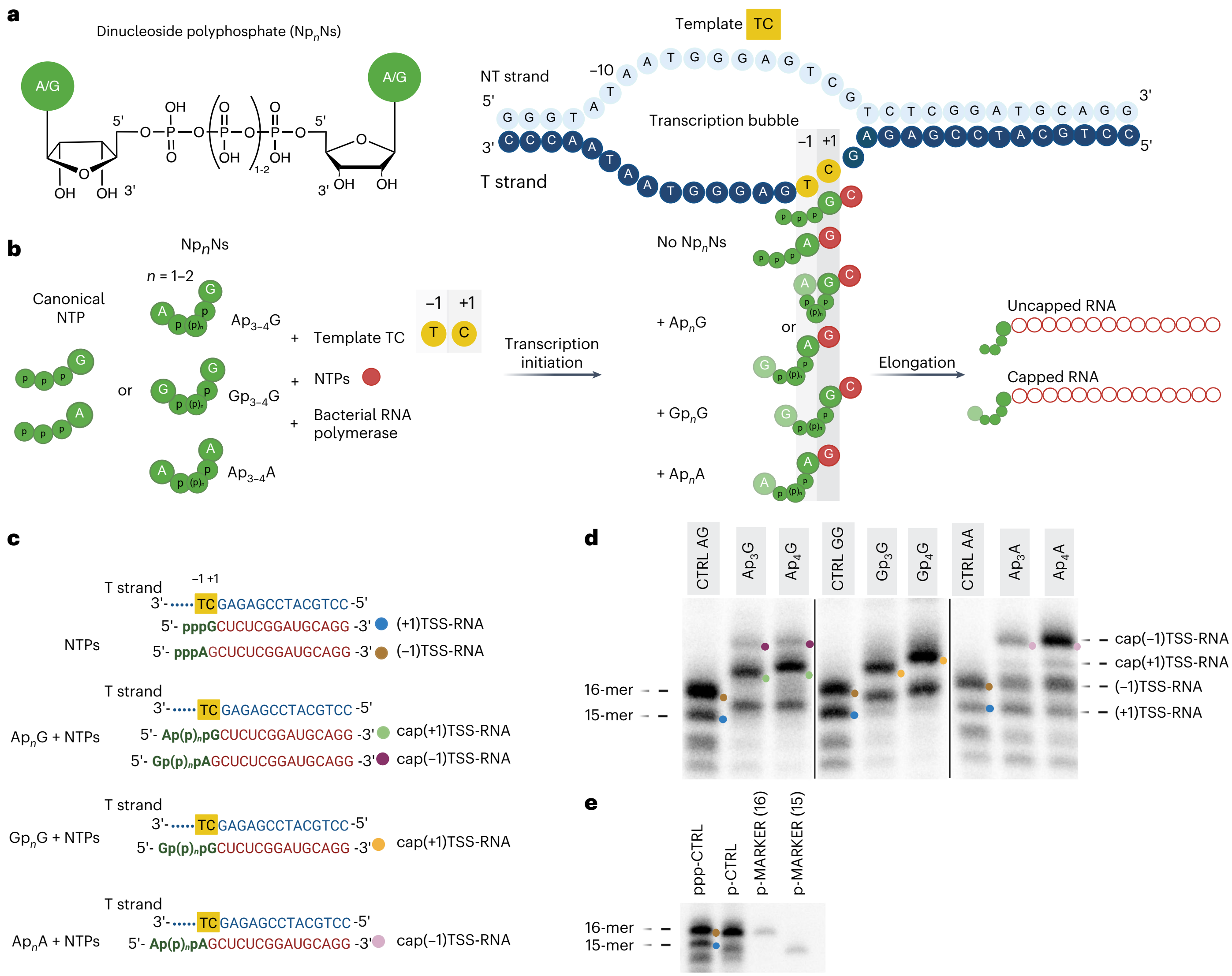

Fig. 1 | IVT reactions with Np$_n$Ns and template TC. a, Chemical structure of Np$_n$Ns. **b**, Schemes of IVT experiments where NTPs or Np$_n$Ns bind to the template TC (with a premelted bubble from position −11 to +2) during transcription initiation with different base-pairing combinations between Np$_n$Ns and the −1 and +1 template strand positions. T, template; NT, nontemplate. **c**, Sequences of color-coded RNA products with and without the addition of Np$_n$Ns. Uncapped 15-mer referred to as (+1)TSS-RNA is indicated by a blue dot, uncapped 16-mer referred to as (−1)TSS-RNA is indicated by a brown dot, capped 15-mers referred to as cap(+1)TSS-RNA are indicated by green and yellow dots and capped 16-mers referred to as cap(−1)TSS-RNA are indicated by purple and pink dots. **d**, PAGE analysis with acryloylaminophenyl boronic acid (APB) showing RNA products obtained from IVT reactions with the template TC and NTPs or their combination with various Np$_n$Ns radiolabeled with α-[^{32}P]CTP. Each control (CTRL AG, CTRL GG, CTRL AA) was designed according to Supplementary Table 2; it shows the migration of the uncapped RNA 15-mer (blue dots) and 16-mer (brown dots) and serves as a molecular weight marker (**e**). The capped products are marked with colored dots according to **c**. The IVT was performed in ten independent experiments; one representative gel is shown. Nonadjacent lanes from the same experiment were rearranged and are separated by delineating black lines. Each lane originates from the same gel. **e**, PAGE (without APB) analysis showing the migration patterns of a 16-mer and 15-mer monophosphate marker along with the triphosphate RNA (ppp-CTRL) and the monophosphate RNA (p-CTRL) generated using template TC and regular NTPs. The markers have the same sequence as the RNA transcript expected from the template TC (Extended Data Table 1), starting at position −1 (p-MARKER(16)) and +1 (p-MARKER(15)). This experiment was performed in triplicate; one representative gel is shown. Created in BioRender. Serianni, V. (2025) https://BioRender.com/p388ku2.

The TC-GTP structure (Extended Data Fig. 8a,b, Supplementary Figs. 4a and 7a and Supplementary Table 7) is similar to crystallographic structures of analogous complexes (PDB 4Q4Z (ref. 37) and PDB 4OIO (ref. 38)). The initiating GTP is bound in the *i* site and the extending CMPcPP in the *i* + 1 site, both canonically base pairing with the TSS +1C and +2G base, respectively. Mg^A is coordinated by the catalytic aspartate triad, whereas Mg^B is only partially coordinated by β′/D739. Notably, there is interpretable density for Mg^{2+} (hereafter Mg^C), which is coordinated by phosphates of the GTP in a tridentate manner. The GTP α and γ phosphates canonically interact with conserved residues[37] β/K838 and K846, and β/Q567 and H999, respectively. Additionally, residue β/Y998 adopts two alternative conformations, one pointing away and one pointing toward the γ phosphate.

In the TC-empty structure (Supplementary Fig. 4a and Extended Data Fig. 8c), we observed that the template strand is antiscrunched[31,33,39] by one nucleotide, placing the template −2G base in line with the *i* − 1 site, the template −1T base in line with the *i* site and the template +1C base in line with the *i* + 1 site, while the +2G base is shifted over the bridge helix toward the downstream DNA duplex (Extended Data Fig. 8c and Supplementary Fig. 8a–c). The nontemplate strand is not shifted in register, which is highlighted by the +2G base of the nontemplate strand bound in the core recognition element

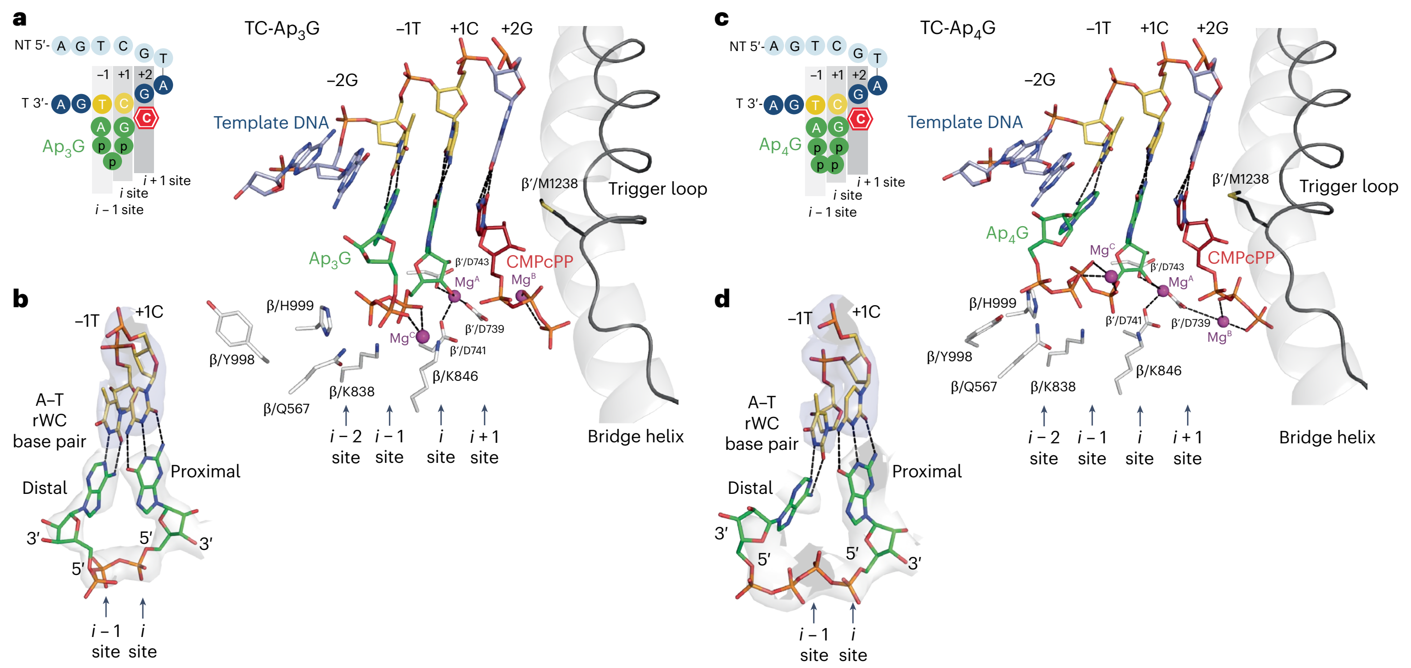

Fig. 2 | Ap$_3$G and Ap$_4$G bound in de novo transcription initiation complexes. **a**, AS structure of de novo transcription initiation, where Ap$_3$G guanine binds canonically in the *i* site and adenine binds noncanonically in the *i* − 1 site. CMPcPP is bound in a preinsertion position in the *i* + 1 site, stabilized by partially closed trigger loop. The DNA template strand is marked with respect to the putative +1 TSS site. The aspartate triad of the AS coordinates Mg$^{\text{A}}$. Conserved residues β/K838 and K846 reach toward the Ap$_3$G α phosphate, β/H999 reaches toward the Ap$_3$G β phosphate, β/Q567 reaches toward the Ap$_3$G γ phosphate and β/Y998 points away from Ap$_3$G. The distal adenine base pair with −1T is sandwiched between the *i* site base pair and −2G. Color coding as in Fig. 1. **b**, Cryo-EM density for Ap$_3$G (gray) and template (blue). The proximal guanine base in the *i* site WC base pairs with template +1C. The distal adenine base in the *i* − 1 site rWC base pairs with template −1T. **c**, AS structure of de novo transcription initiation, where Ap$_4$G guanine binds canonically in the *i* site and adenine binds noncanonically in the *i* − 1 site. The depiction is analogous to **a**. β′/D739 coordinates both Mg$^{\text{A}}$ and Mg$^{\text{B}}$. Conserved residues β/K838 and K846 reach toward the Ap$_4$G α phosphate, whereas conserved residues β/Q567 and β/H999 reach toward the Ap$_4$G γ and δ phosphates; β/Y998 points toward the Ap$_4$G δ phosphate. **d**, Cryo-EM density for Ap$_4$G (gray) and template (blue). The proximal guanine base in the *i* site WC base pairs with template +1C. The cryo-EM density for the distal part of Ap$_4$G is less well defined. The adenine base in the *i* − 1 site rWC base pairs with template −1T.

(CRE)-specific binding pocket of RNAP[27] (Supplementary Fig. 8a–c). As the AS is unoccupied, the antiscrunching of the template by one nucleotide and the concomitant TSS shift happens without any stabilization by nucleotides pairing with the antiscrunched template. This template oscillation[32] then allows the use of both +1 and −1 TSS in the IVT reactions in our in vitro system. Altogether, the TC-GTP and TC-empty structures set a basis for structural comparison of complexes with various bound Np$_n$Ns visualized in this study.

Distal base binds template in a reverse WC (rWC) manner

Next, we visualized the same template TC holoenzyme complex with Ap$_3$G and CMPcPP, hereafter referred to as TC-Ap$_3$G (Fig. 2a,b, Supplementary Figs. 4b and 7b and Supplementary Table 7). Like in the TC-GTP structure, the CMPcPP in the *i* + 1 site base pairs with the +2G base in a preinsertion position. The guanosine of Ap$_3$G in the *i* site base pairs canonically with the +1C TSS (hereafter, we call the nucleoside of Np$_n$N in the *i* site proximal; Fig. 2b). The guanosine is, thus, aligned for the first nucleotidyl transfer reaction. The α phosphate (counted from the proximal nucleoside) is positioned by β/K838 and β/K846 in a similar way to GTP in the TC-GTP structure. The β phosphate (instead of the γ phosphate in TC-GTP) is positioned by β/H999 and the γ phosphate is positioned by β/Q567; β/Y998 points away from Ap$_3$G. There is an interpretable density for Mg$^{\text{C}}$ coordinated by the α and γ phosphates of Ap$_3$G. The torsion angles between the γ phosphate and the adjacent ribose moiety direct the adenosine into the *i* − 1 position to base pair with the template −1T (hereafter, we call the nucleoside of Np$_n$N in the *i* − 1 site distal). The glycosidic bond of the distal adenosine is in the *trans* orientation and the adenine base pairs with the −1T base in an rWC manner (Extended Data Fig. 9a). This is in contrast to the *cis* orientation in regular RNA–DNA[27] or 5′-end hydroxyl dinucleotide primer–DNA duplexes[15] (Extended Data Fig. 9b). The cryo-EM density (Fig. 2b and Supplementary Fig. 7b) does not support other potential noncanonical base-pairing options such as the Hoogsteen mode. The base pair in the *i* − 1 site is further stabilized by stacking interactions with the base pair in the *i* site from one side and from the other with the template purine base −2G in line with the *i* − 2 site, which overlaps with both the template −1T and the distal adenine base of Ap$_3$G. Such stacking stabilization by a purine template base in line with the *i* − 2 site was previously observed for nascent dinucleotide RNA[27] and 5′-end hydroxyl dinucleotide primers[15].

In summary, the proximal guanosine in the *i* site binds canonically in the RNAP AS to enable the initial nucleotidyl transfer. The 5′-to-5′ triphosphate linker towards the distal adenosine does not allow for the regular *cis* orientation of the ribose that would enable canonical base pairing with the template; instead, the ribose adopts a *trans* conformation and the distal adenosine base pairs in a rWC manner.

Ap$_4$G tetraphosphate linker allows distal base rWC pairing

In the next step, we aimed to structurally visualize the effect of the tetraphosphate linker of Ap$_4$G on binding to the RNAP AS. We reconstituted the template TC holoenzyme complex with Ap$_4$G and CMPcPP and obtained a reconstruction hereafter referred to as TC-Ap$_4$G (Fig. 2c,d, Supplementary Figs. 4c and 7c and Supplementary Table 7). The CMPcPP and the proximal guanosine of Ap$_4$G are canonically bound, aligned for the first nucleotidyl transfer reaction. The α phosphate is canonically positioned by β/K838 and β/K846 and the γ and δ phosphates are in close proximity to β/H999 and β/Q567. Additionally, in contrast to TC-Ap$_3$G, residue β/Y998 points toward the δ phosphate group of the

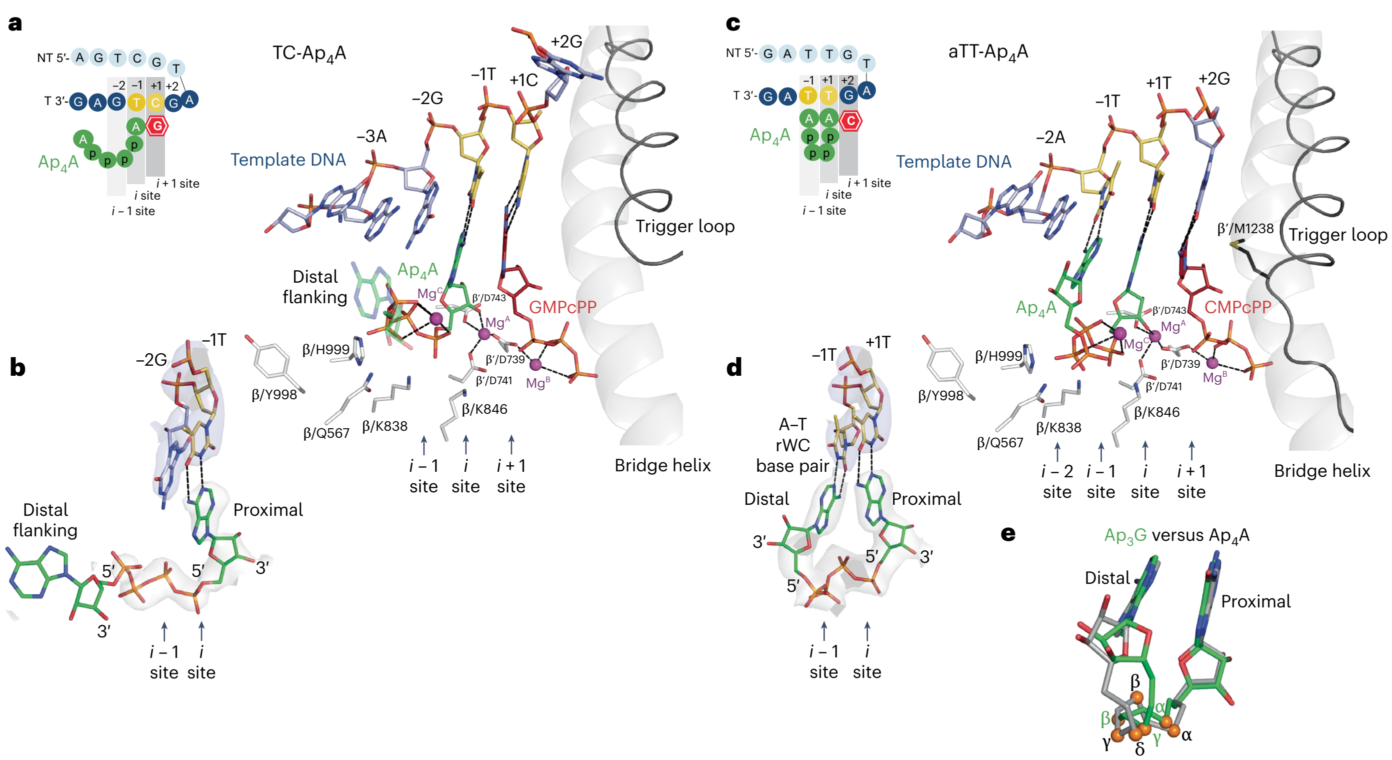

Fig. 3 | Ap$_4$A bound in de novo transcription initiation complexes. a, AS structure of de novo transcription initiation, where Ap$_4$A proximal adenine binds canonically in the *i* site. GMPcPP is bound in a preinsertion position in the *i* + 1 site. The DNA template strand is antiscrunched by one nucleotide relative to the AS and to the nontemplate strand. The aspartate triad of the AS coordinates Mg^A and β′/D739 coordinates Mg^B. Conserved residues β/K838 and K846 reach toward the Ap$_4$A α phosphate and β/H999 and Q567 reach towards the Ap$_4$A γ phosphate; β/Y998 points away from Ap$_4$A. The distal adenine does not base pair with the −2G base of the template in the *i* − 1 site and flanks. Color coding as in Fig. 1. **b**, Cryo-EM density for Ap$_4$A (gray) and template (blue). The proximal adenine base in the *i* site WC base pairs with template −1T. The distal adenine base flanks. **c**, AS structure of de novo transcription initiation, where Ap$_4$A proximal adenine binds canonically in the *i* site and the distal adenine binds noncanonically in the *i* − 1 site. The depiction is analogous to **a**. Conserved residues β/K838 and K846 reach toward the Ap$_4$A α phosphate, H999 reaches toward the Ap$_4$A γ phosphate and β/Q567 reaches toward both γ and δ phosphates of the Ap$_4$A; β/Y998 points away from Ap$_4$A. **d**, Cryo-EM density for Ap$_4$A (gray) and template (blue). The proximal adenine base in the *i* site WC base pairs with template +1T. The distal adenine base in the *i* − 1 site rWC base pairs with template −1T. **e**, Comparison of triphosphate and tetraphosphate linkers in TC-Ap$_3$G (green) and aTT-Ap$_4$A (gray) structures. Phosphorus atoms are highlighted as orange spheres. Nonbridging oxygen atoms of phosphates are omitted for clarity.

Ap$_4$G tetraphosphate linker, although a weak map for the alternative conformation pointing away from Ap$_4$G is also present. However, the cryo-EM density for the δ phosphate, the distal ribose and the adenine base is less well defined (Fig. 2d and Supplementary Fig. 7c). Nevertheless, the distal ribose clearly adopts the *trans* orientation relative to the template −1T and the distal adenine base pairs in the rWC manner with the −1T base of the template, stabilized further by stacking with the −2G base (Fig. 2c).

Taken together, the results confirm that the proximal moiety of Ap$_4$G is aligned for the transcription initiation reaction but the effect of the tetraphosphate linker on the binding of the distal part of the Ap$_4$G could not be resolved in detail in the TC-Ap$_4$G structure. We, therefore, set out to visualize the tetraphosphate linker and the distal nucleoside binding using Ap$_4$A.

Distal base of Ap$_4$A does not require base pairing

The transcription reaction initiating with Ap$_4$A on the TC template yielded a capped product (Fig. 1c,d) starting from the −1T template position as the TSS, instead of the putative +1C TSS position, confirmed by LC–MS (Extended Data Fig. 2 and Supplementary Table 3). Reconstitution of the TC template holoenzyme complex with Ap$_4$A and GMPcPP yielded a reconstruction hereafter referred to as TC-Ap$_4$A (Fig. 3a,b, Supplementary Figs. 4d and 7d and Supplementary Table 7). In this structure, indeed, the template strand is antiscrunched[31–33,39] by one nucleotide, like in the TC-empty structure (Extended Data Fig. 8c), placing the template −2G base in line with the *i* − 1 site, the template −1T base in line with the *i* site and the template +1C base in line with the *i* + 1 site (Supplementary Fig. 8d,e). The GMPcPP and the proximal adenosine of Ap$_4$A are canonically paired in the *i* + 1 site with the +1C base and in the *i* site with the −1T base, respectively (Fig. 3a and Supplementary Fig. 7d). The distal adenosine of Ap$_4$A does not base pair with the bulky −2G purine residue in the *i* − 1 site and is, therefore, flanking into the void of the AS cavity toward σ^A region 3.2. There is only a blurred density for the distal ribose (Fig. 3b) and no defined density for the distal base, suggesting that there is no contact with σ^A region 3.2. The base pair in the *i* site is stabilized by a stacking interaction with the −2G base in line with the *i* − 1 site. This type of stacking has already been reported to occur during stabilization of the first initiation NTP (iNTP) binding in the initiation complex[37]. Similarly, the interaction of the Ap$_4$A proximal base is sufficient to retain it in the AS, even without additional stabilization from pairing of the distal nucleoside base of Ap$_4$A at the *i* − 1 site. The tetraphosphate linker is stabilized by the canonical interaction of α and γ phosphates with conserved residues β/K838 and K846, and β/H999 and Q567, respectively. The mutual orientation of the phosphates is also stabilized by the coordination of Mg^C, engaging all four phosphates.

In summary, the inherent capability of the TC template strand to antiscrunch in the AS by one nucleotide enabled the Ap$_4$A to canonically bind in the *i* site. The purine incompatibility at the *i* − 1 site, however, forces the distal base of Ap$_4$A to flank. Nevertheless, such an Ap$_4$A initiation complex is stable enough for the transcription reaction to proceed.

Ap_4A can base pair using both proximal and distal nucleosides

To visualize the pairing of Ap_4A nucleosides in both *i* and *i* − 1 sites, we attempted to reconstruct the holoenzyme complex with Ap_4A, GMPcPP and a modified template tTC (Extended Data Table 1) that would place the T base in line with the *i* − 1 site after template antiscrunching. However, even though the template was positioned as expected, we could only visualize blurred contours of Ap_4A and GMPcPP in the AS. We, therefore, created the aTT template (Extended Data Table 1 and Supplementary Fig. 4e), which featured a transcription bubble shortened by one base to prevent antiscrunching and was still compatible with IVT reactions (Supplementary Fig. 9). We expected that this template would position the +1T and −1T bases in line with the *i* and *i* − 1 sites, respectively, to achieve full base pairing with Ap_4A; the +2G base would be in line with the *i* + 1 site to base pair with CMPcPP. The resulting structure, hereafter referred to as aTT-Ap_4A (Fig. 3c,d, Supplementary Fig. 7e and Supplementary Table 7), indeed visualized CMPcPP and the proximal adenosine of Ap_4A canonically bound in the *i* + 1 and *i* sites, respectively (Fig. 3c). The cryo-EM density was clearly defined for the tetraphosphate linker and for the distal adenosine base pairing with the −1T base of the template in the *i* − 1 site (Fig. 3d and Supplementary Fig. 7e). The α phosphate is canonically positioned by β/K838 and β/K846. Residue β/H999 reaches toward the γ phosphate, which itself interacts with β/Q567. The cryo-EM map for residue β/Y998 indicates two alternative conformations, pointing away and toward Ap_4A; however, the conformation pointing away from Ap_4A prevails. Concomitantly, the δ phosphate of Ap_4A in aTT-Ap_4A adopts a different position in comparison to Ap_4G in TC-Ap_4G. The β and α phosphates together coordinate Mg^C. The relatively loosely defined distal ribose adopts a *trans* orientation relative to the −1T template base, with the distal adenine forming an rWC pair with −1T, as supported by the cryo-EM map (Fig. 3d and Supplementary Fig. 7e). The distal adenine base is also stabilized in the base pair with −1T by stacking interactions with the −2A purine base of the template in line with the *i* − 2 site. The distal adenine binds similarly to the −1T template base in both TC-Ap_3G and aTT-Ap_4A (Fig. 3e; root mean square deviation of the distal base = 0.421 Å). Intriguingly, it appears that the binding conformations of the two bases in Np_nNs are constant and that it is the conformation of the triphosphate or tetraphosphate linker that needs to adjust in between proximal and distal nucleosides.

In all our structures, when base pairing, the distal adenosine in the *i* − 1 site features ribose in the *trans* orientation relative to the template in line with the *i* − 1 site, which forces the distal adenosine to rWC base pair with the template base in line with the *i* − 1 site. We, therefore, conclude that the rWC mode is the preferred binding mode of the distal adenosine, induced by the spatial constrains of the 5′-to-5′ triphosphate or tetraphosphate linker between the ribose of the proximal nucleoside and that of the distal nucleoside.

Discussion

In this article, we describe the molecular details of 5′ RNA capping with Np_nNs by bacterial RNAP. We confirm previous observations[11,19] that Np_nNs are used as NCINs in IVT reactions using bacterial RNAP (in our case, *Tt* RNAP). As anticipated, Np_nNs readily initiate with the proximal base at the putative +1 TSS of a DNA promoter when canonical base pairing is available. In our in vitro system, using artificial promoters with preformed transcription bubbles (Fig. 1b and Extended Data Table 1), the template strand TSS can oscillate between the +1 and −1 positions (Supplementary Fig. 4a, Extended Data Fig. 8 and Supplementary Fig. 8). When the putative +1 TSS is not compatible with canonical base pairing with the proximal base of Np_nNs, the −1 position, where canonical base pairing is possible, is readily used as the TSS instead. This leads to the formation of capped RNA longer by one nucleotide. We observe this TSS shift, for example, with $Ap_{3\text{-}4}A$ initiating at the −1T position of the TC template (Fig. 1d) as confirmed by the detection of the cap(−1)TSS-RNA product in our LC–MS analyses (Extended Data Fig. 2 and Supplementary Table 3). Furthermore, we observed the TSS shift for other combinations of Np_nNs and templates (Extended Data Figs. 4–7 and Supplementary Tables 5 and 6), demonstrating that this is a general behavior of this particular set of artificial DNA promoters with preformed transcription bubbles. As only limited information[19] is available on natural RNA sequences capped by Np_nNs, it is difficult to study this behavior in the context of native DNA promoters. To assess Np_nN capping under more native-like conditions, we developed an IVT assay using a supercoiled plasmid with a fully complementary DNA promoter. PAGE and LC–MS analyses combined with RNase A treatment confirmed that *Tt* RNAP generates all Np_nN-capped RNAs from this standard template, initiating transcription from both +1 and −1 positions as TSSs (Extended Data Fig. 3 and Supplementary Table 4).

Next, to characterize Np_nNs as NCINs, we visualized the initial binding of Np_nNs into the RNAP AS just before the first nucleotidyl transfer reaction. In a series of cryo-EM structures, we captured the RNAP AS, where NCINs align to react with the first extending nucleotide. The structures reveal how Np_nNs bind to the *i* and *i* − 1 sites of the RNAP AS and how they base pair with the promoter template strand. Expectedly, the proximal G or A of either Ap_nG or Ap_nA base pairs with the template in line with the *i* site in a canonical WC manner to align with the RNAP AS to react with the extending nucleotide. The distal nucleoside either base pairs in line with the *i* − 1 site or flanks into the AS cavity. Importantly, the base pairing of the distal base is not canonical because of the presence of the 5′-to-5′ triphosphate or tetraphosphate linker between the two nucleosides, instead of a 5′-to-3′ single phosphate in a regular RNA product[15] (Extended Data Figs. 1 and 9). The orientation of the distal and proximal ribose of the Np_nNs resulting from the 5′-to-5′ linkage does not allow the canonical *cis* conformation of the distal ribose aligned with the *i* − 1 site but instead dictates a *trans* conformation. The *trans* conformation is then compatible with the rWC base pairing of the distal nucleoside. The rWC-pairing distal bases in both TC-Ap_3G and aTT-Ap_4A adopt similar binding poses (Fig. 3e), likely facilitated by conformational adjustment of the flexible triphosphate or tetraphosphate linker between the proximal and distal nucleosides. In addition, we also conclude that, when there is a bulky purine template base in line with the *i* − 1 site, such as the −2G base in the antiscrunched template TC, the distal purine nucleoside of Np_4N does not form any noncanonical purine–purine base pair because of steric hindrance and is forced to flank. In other words, two bulky purines cannot be accommodated opposite each other.

One of the best known noncanonical RNA caps is NAD, which has also been detected in various bacterial RNAs[3,18,40,41]. However, the incorporation efficiency of NAD as an NCIN is only about one seventh of that of ATP[19]. Nevertheless, we wanted to compare the incorporation efficiency of NAD by *Tt* RNAP with Np_nNs. Expectedly, our efforts to use NAD as NCIN produced only traces of NAD-RNA (Supplementary Fig. 3) and these experiments confirmed that NAD is indeed a much less potent NCIN than NTPs and Np_nNs. Our attempts to visualize NAD binding to the *i* and *i* − 1 sites of the RNAP AS by cryo-EM have failed. Therefore, we can only compare Np_nN binding at the *i* and *i* − 1 sites to NAD binding at the *i* − 1 and *i* − 2 sites, as visualized in the RNAP complex with NAD-pC trinucleotide (PDB 5D4D; Extended Data Fig. 9d).

The *Tt* RNAP is a well-established representative of the RNAP AS, conserved across all cellular RNAPs[37,42]; therefore, it can be used as a model to study interactions of Np_nNs with the RNAP itself. However, apart from the conserved residues β/K838, K846, H999 and Q567, which contact the phosphate groups of both the canonical iNTPs and Np_nNs as NCINs, we only identified β/Y998 as a potential additional interacting residue (Fig. 2c and Extended Data Fig. 8a). The alternative conformation of β/Y998 pointing toward the NCIN might potentially interact with the δ phosphate group in the case of the tetraphosphate linker, as observed in the TC-Ap_4G structure. However, given the low occupancy of this β/Y998 conformer in the structures with Ap_4A, it does not seem to be critical for tetraphosphate linker binding into the RNAP AS. Surprisingly, we observed an Mg^C cation coordinated by the triphosphate or tetraphosphate of iNTPs or Np_nNs. Mg^C does not specifically interact with the RNAP protein and we propose that it serves as a countercharge to the phosphate groups.

The only determinant of how Np_nNs bind in the RNAP AS seems to be the DNA promoter sequence at the +1 and −1 template positions aligned in the *i* and *i* − 1 sites, respectively. A strict requirement is canonical WC compatibility in the *i* site. In our in vitro system, we observe that the template strand can be antiscrunched, thereby shifting the TSS by one position (Extended Data Fig. 8c and Supplementary Figs. 4a and 8). Intriguingly, in the case of the TC-Ap_4A structure (Supplementary Fig. 4d), the base identity of Ap_4A favored the antiscrunched TSS template strand position to canonically bind in the *i* site. As Np_nNs have two 3′ hydroxyl groups available for initiation on both termini of the molecule, Ap_nGs use both termini in our IVT reactions. The selection of the proximal base (A or G) in the *i* site follows the base identity requirements in the TSS.

The incorporation of Np_nNs as NCINs increases the efficiency of transcription initiation in comparison to regular iNTPs[19,20]. Furthermore, template pyrimidine bases at the *i* − 1 site increase the efficiency of Np_nNs noncanonical transcription initiation, one of the explanations being potential WC base pairing[19]. Our structure analysis revealed rWC base pairing of the T pyrimidine base at the *i* − 1 site. Nevertheless, transcription initiation with template TC and Ap_4A is efficient (Fig. 1d) despite the lack of base pairing at the *i* − 1 site with the bulky purine −2G (Fig. 3a,b). On the other hand, −2G stabilizes the proximal base pair by a stacking interaction. Our structural data on the very first step of transcription initiation, thus, do not provide any clear mechanistic explanation of the observed[19] increase in transcription initiation efficiency caused by pyrimidine bases aligned with the *i* − 1 site. Future structural studies of subsequent transcription steps might provide a deeper understanding.

In summary, we present molecular details of how Np_nNs bind into the AS of RNAP at the very beginning of transcription, which demonstrate how Np_nNs function as versatile and efficient NCIN. Given the conservation of the Np_nN-binding region in the RNAP AS, we presume that the here-described modes of Np_nNs binding will be found to be universal for other cellular RNAPs, including eukaryotic polymerase II.

Online content

Any methods, additional references, Nature Portfolio reporting summaries, source data, extended data, supplementary information, acknowledgements, peer review information; details of author contributions and competing interests; and statements of data and code availability are available at https://doi.org/10.1038/s41589-025-02134-5.

References

1. Cappannini, A. et al. MODOMICS: a database of RNA modifications and related information. 2023 update. *Nucleic Acids Res.* **52**, D239–D244 (2024).
2. Chen, Y. G., Kowtoniuk, W. E., Agarwal, I., Shen, Y. & Liu, D. R. LC/MS analysis of cellular RNA reveals NAD-linked RNA. *Nat. Chem. Biol.* **5**, 879–881 (2009).
3. Cahova, H., Winz, M.-L., Hoefer, K., Nuebel, G. & Jaeschke, A. NAD captureSeq indicates NAD as a bacterial cap for a subset of regulatory RNAs. *Nature* **519**, 374–377 (2015).
4. Winz, M.-L. et al. Capture and sequencing of NAD-capped RNA sequences with NAD captureSeq. *Nat. Protoc.* **12**, 122 (2016).
5. Jiao, X. et al. 5′ end nicotinamide adenine dinucleotide cap in human cells promotes RNA decay through DXO-mediated deNADding. *Cell* **168**, 1015–1027 (2017).
6. Kowtoniuk, W. E., Shen, Y., Heemstra, J. M., Agarwal, I. & Liu, D. R. A chemical screen for biological small molecule–RNA conjugates reveals CoA-linked RNA. *Proc. Natl Acad. Sci. USA* **106**, 7768–7773 (2009).
7. Sherwood, A. V. et al. Hepatitis C virus RNA is 5′-capped with flavin adenine dinucleotide. *Nature* **619**, 811–818 (2023).
8. Wang, J. et al. Quantifying the RNA cap epitranscriptome reveals novel caps in cellular and viral RNA. *Nucleic Acids Res.* **47**, e130 (2019).
9. Julius, C. & Yuzenkova, Y. Bacterial RNA polymerase caps RNA with various cofactors and cell wall precursors. *Nucleic Acids Res.* **45**, 8282–8290 (2017).
10. Luciano, D. J., Levenson-Palmer, R. & Belasco, J. G. Stresses that raise Np4A levels induce protective nucleoside tetraphosphate capping of bacterial RNA. *Mol. Cell* **75**, 957–966 (2019).
11. Hudeček, O. et al. Dinucleoside polyphosphates act as 5′-RNA caps in bacteria. *Nat. Commun.* **11**, 1052 (2020).
12. František Potužník, J. et al. Diadenosine tetraphosphate (Ap4A) serves as a 5′ RNA cap in mammalian cells. *Angew. Chem. Int. Ed. Engl.* **63**, e202314951 (2024).
13. Potužník, J. F. & Cahova, H. If the 5′ cap fits (wear it)—non-canonical RNA capping. *RNA Biol.* **21**, 1–13 (2024).
14. Vvedenskaya, I. O. et al. Growth phase-dependent control of transcription start site selection and gene expression by nanoRNAs. *Genes Dev.* **26**, 1498–1507 (2012).
15. Skalenko, K. S. et al. Promoter-sequence determinants and structural basis of primer-dependent transcription initiation in *Escherichia coli*. *Proc. Natl Acad. Sci. USA* **118**, e2106388118 (2021).
16. Malygin, A. G. & Shemyakin, M. F. Adenosine, NAD and FAD can initiate template-dependent RNA a synthesis catalyzed by *Escherichia coli* RNA polymerase. *FEBS Lett.* **102**, 51–54 (1979).
17. Huang, F. Efficient incorporation of CoA, NAD and FAD into RNA by in vitro transcription. *Nucleic Acids Res.* **31**, e8 (2003).
18. Bird, J. G. et al. The mechanism of RNA 5′ capping with NAD^+, NADH and desphospho-CoA. *Nature* **535**, 444–447 (2016).
19. Luciano, D. J. & Belasco, J. G. Np(4)A alarmones function in bacteria as precursors to RNA caps. *Proc. Natl Acad. Sci. USA* **117**, 3560–3567 (2020).
20. Benoni, R., Culka, M., Hudeček, O., Gahurova, L. & Cahová, H. Dinucleoside polyphosphates as RNA building blocks with pairing ability in transcription initiation. *ACS Chem. Biol.* **15**, 1765–1772 (2020).
21. Despotović, D. et al. Diadenosine tetraphosphate (Ap4A)—an *E. coli* alarmone or a damage metabolite? *FEBS J.* **284**, 2194–2215 (2017).
22. Ji, X. et al. Alarmone Ap4A is elevated by aminoglycoside antibiotics and enhances their bactericidal activity. *Proc. Natl Acad. Sci. USA* **116**, 9578–9585 (2019).
23. Kimura, Y., Tanaka, C., Sasaki, K. & Sasaki, M. High concentrations of intracellular Ap4A and/or Ap5A in developing *Myxococcus xanthus* cells inhibit sporulation. *Microbiology (Reading)* **163**, 86–93 (2017).
24. Paget, M. S. B. & Helmann, J. D. The σ70 family of sigma factors. *Genome Biol.* **4**, 203 (2003).
25. Saecker, R. M., Record, M. T. Jr. & Dehaseth, P. L. Mechanism of bacterial transcription initiation: RNA polymerase–promoter binding, isomerization to initiation-competent open complexes, and initiation of RNA synthesis. *J. Mol. Biol.* **412**, 754–771 (2011).
26. Zhang, G. et al. Crystal structure of *Thermus aquaticus* core RNA polymerase at 3.3 Å resolution. *Cell* **98**, 811–824 (1999).
27. Zhang, Y. et al. Structural basis of transcription initiation. *Science* **338**, 1076–1080 (2012).
28. Shi, J. et al. Structural basis of Mfd-dependent transcription termination. *Nucleic Acids Res.* **48**, 11762–11772 (2020).
29. Triana-Alonso, F. J., Dabrowski, M., Wadzack, J. & Nierhaus, K. H. Self-coded 3′-extension of run-off transcripts produces aberrant products during in vitro transcription with T7 RNA polymerase. *J. Biol. Chem.* **270**, 6298–6307 (1995).

30. Goldman, S. R., Ebright, R. H. & Nickels, B. E. Direct detection of abortive RNA transcripts in vivo. *Science* **324**, 927–928 (2009).
31. Winkelman, J. T. et al. Multiplexed protein-DNA cross-linking: scrunching in transcription start site selection. *Science* **351**, 1090–1093 (2016).
32. Yu, L. et al. The mechanism of variability in transcription start site selection. *eLife* **6**, e32038 (2017).
33. Robb, N. C. et al. The transcription bubble of the RNA polymerase-promoter open complex exhibits conformational heterogeneity and millisecond-scale dynamics: implications for transcription start-site selection. *J. Mol. Biol.* **425**, 875–885 (2013).
34. Miller, M. L. & Miller, D. L. Non-DNA-templated addition of nucleotides to the 3′ end of RNAs by the mitochondrial RNA polymerase of *Physarum polycephalum*. *Mol. Cell. Biol.* **28**, 5795–5802 (2008).
35. Cheng, Y. W., Visomirski-Robic, L. M. & Gott, J. M. Non-templated addition of nucleotides to the 3′ end of nascent RNA during RNA editing in *Physarum*. *EMBO J.* **20**, 1405–1414 (2001).
36. Krásný, L. & Gourse, R. L. An alternative strategy for bacterial ribosome synthesis: *Bacillus subtilis* rRNA transcription regulation. *EMBO J.* **23**, 4473–4483 (2004).
37. Basu, R. S. et al. Structural basis of transcription initiation by bacterial RNA polymerase holoenzyme. *J. Biol. Chem.* **289**, 24549–24559 (2014).
38. Zhang, Y. et al. GE23077 binds to the RNA polymerase '*i*' and '*i*+1' sites and prevents the binding of initiating nucleotides. *eLife* **3**, e02450 (2014).
39. Vvedenskaya, I. O. et al. Massively systematic transcript end readout, 'MASTER': transcription start site selection, transcriptional slippage, and transcript yields. *Mol. Cell* **60**, 953–965 (2015).
40. Morales-Filloy, H. G. et al. The 5′-NAD cap of RNAIII modulates toxin production in *Staphylococcus* aureus isolates. *J. Bacteriol.* **202**, e00591-19 (2019).
41. Frindert, J. et al. Identification, biosynthesis, and decapping of NAD-capped RNAs in *B. subtilis*. *Cell Rep.* **24**, 1890–1901 (2018).
42. Ebright, R. H. RNA polymerase: structural similarities between bacterial RNA polymerase and eukaryotic RNA polymerase II. *J. Mol. Biol.* **304**, 687–698 (2000).

Methods

Unless mentioned otherwise in the text, the chemicals used were purchased from Merck chemicals. If available, the chemicals were of molecular biology grade. Oligonucleotides were purchased from Generi Biotech. DNA scaffolds were prepared using two oligonucleotides (template strand and nontemplate strand) and annealed in a total volume of 240 µl containing 33 µM each oligonucleotide, 10 mM Tris pH 7.8, 50 mM NaCl and 1 mM EDTA. Samples were heated to 90 °C for 5 min, after which the temperature gradually decreased to 20 °C in 2 h. All templates are listed in Supplementary Table 1.

Tt RNAP holoenzyme expression and purification

As previously described[26], purification of the RNAP holoenzyme poses difficulties caused by its unstable σ^A subunit that is susceptible to proteolysis. To prevent sample heterogeneity, we isolated the native RNAP core from *T. thermophilus* and complexed it with a recombinantly expressed σ^A subunit to obtain a homogeneous preparation of the RNAP holoenzyme.

For isolation of the RNAP core, *Tt* HB8 (DSM579, German Collection of Microorganisms and Cell Cultures) cells were grown at 75 °C in a medium containing 4 g l^{-1} yeast extract, 8 g l^{-1} proteose peptone no. 3 and 2 g l^{-1} NaCl at pH 7.0. Cells were harvested after 20 h of cultivation, resuspended in lysis buffer (20 mM Tris-HCl pH 8.7, 50 mM NaCl, 10 mM EDTA, 10 mM β-mercaptoethanol and 0.1 mM PMSF), disrupted using an EmulsiFlex-C3 cell disrupter (Avestin) and centrifuged at 20,000*g*. The resulting cell lysate was applied to a Q-Sepharose high-performance column (Cytiva) equilibrated in lysis buffer. The column was washed with lysis buffer and eluted with a seven-step gradient of sodium chloride (0.15–1 M). Fractions containing the RNAP core were collected and concentrated using Amicon Ultra centrifugal units (30-kDa molecular weight cutoff (MWCO); Merck Life Sciences). This step is crucial because it facilitates the removal of most of the DNA from the sample, allowing it to efficiently bind to the Mono-Q column in the next step. Each sample was then dialyzed into buffer A (20 mM Tris-HCl pH 8.7, 50 mM NaCl, 5 mM β-mercaptoethanol and 1 mM EDTA) and loaded onto a Mono-Q 5/50 GL column (Cytiva) equilibrated in buffer A. The column was washed with buffer A and eluted with a linear gradient of sodium chloride (0.05–1 M). Each sample was subsequently concentrated and loaded onto a Superdex 200 10/300 GL column (Cytiva) with a running buffer containing 25 mM Tris-HCl pH 8.7, 200 mM NaCl and 5% glycerol. Fractions containing the RNAP core were concentrated to 1 mg ml^{-1} and stored at −80 °C.

The σ^A subunit synthetic gene was subcloned into the pMCSG7 vector (T7 promoter-driven, originally designed for ligation-independent cloning[43]). The vector was first modified by a sequence coding for the N-terminal His_6 tag, followed by a sequence coding for the tobacco etch virus protease cleavage site with additional amino acid residues (SNAAS). The σ^A subunit coding sequence was cloned as an NheI–EcoRI insert into this modified vector. The protein was overexpressed in the *E. coli* strain BL21 (DE3) (New England Biolabs (NEB)) at 37 °C in LB medium supplemented with 0.8% glycerol and 100 µg ml^{-1} ampicillin. Subsequently, σ^A expression was induced at an optical density at 600 nm of 0.6 by addition of ETG to the final concentration of 1 mM and cells were further cultivated for 3 h before they were harvested by centrifugation. Cells were resuspended in ten volumes of lysis buffer (50 mM Tris-HCl pH 7.9, 200 mM NaCl, 10 mM β-mercaptoethanol and 5% glycerol) containing protease inhibitors (cOmplete EDTA-free, Roche) and lysed using an EmulsiFlex-C3 cell disrupter (Avestin). The cell lysate was clarified by centrifugation at 20,000*g* and loaded onto a 5-ml HisTrap Ni-NTA column equilibrated in lysis buffer. The column was washed with lysis buffer supplemented with 10 mM imidazole and the protein was eluted in three steps with lysis buffer containing 50, 250 and 500 mM imidazole. Fractions containing the σ^A subunit were collected and concentrated using Amicon Ultra centrifugal units (30-kDa MWCO; Merck Life Sciences). The last purification step involved gel filtration on a Superdex 200 10/300 GL column (Cytiva) in a running buffer containing 50 mM Tris-HCl pH 7.9, 200 mM NaCl, 10 mM β-mercaptoethanol and 5% glycerol. The purified σ^A protein was concentrated to 13 mg ml^{-1} and stored at −80 °C. The purification yield was 7.8 mg of protein from 1 l of bacterial culture with the purity assessed by silver-stained SDS–PAGE to be greater than 95%.

To prepare the holoenzyme complex, the σ^A subunit was transferred into a buffer containing 20 mM Tris-HCl pH 8.7, 100 mM NaCl and 5% β-mercaptoethanol, mixed with the RNAP core in a 4:1 molar ratio and incubated overnight at 4 °C. The mixture was then applied to a Superdex 200 10/300 GL column (Cytiva) equilibrated in 20 mM Tris-HCl pH 8.7, 100 mM NaCl and 1% glycerol. In this step, the excess of the σ^A subunit was separated from the RNAP holoenzyme, as verified by SDS–PAGE analysis (Supplementary Fig. 10). Fractions containing the RNAP holoenzyme were pooled, concentrated to a final concentration of 1 mg ml^{-1} using Amicon Ultra centrifugal units (30-kDa MWCO, Merck Life Sciences) and stored at −80 °C.

IVT with *Tt* RNAP

IVT was performed in a reaction volume of 25 µl containing 2 µM template DNA (Supplementary Table 1), 0.6 mM ATP, 0.6 mM GTP, 0.6 mM UTP, 0.4 mM CTP and 0.2 µl of α-[^{32}P]CTP (activity: 9.25 MBq in 25 µl), 1.6 mM Np_nNs (Ap_3A, Ap_4A, Ap_3G, Ap_4G, Gp_3G and Gp_4G; Jena Bioscience) or NAD in different concentrations (0.6 mM, 1.6 mM, 3.2 mM and 6.4 mM), 50 mM Tris-HCl pH 7.9, 100 mM KCl, 10 mM $MgCl_2$, 1 mM DTT, 5 µg ml^{-1} BSA, 5% glycerol and 96 nM *Tt* RNAP. In negative controls, Np_nNs were replaced with appropriate regular NTPs ATP and/or GTP (Supplementary Table 2). The concentration of ATP was 2.2 mM in the negative controls for the samples containing Ap_nA as starting nucleotides. The concentration of GTP was 2.2 mM in the negative controls for the samples containing Gp_nG as starting nucleotides. The concentration of ATP and GTP was 1.4 mM each in the negative controls for the samples containing Ap_nG as starting nucleotides (Supplementary Table 2). The IVT mixture was incubated for 2 h at 65 °C.

DNAse treatment of in vitro transcripts

To obtain pure RNA, the DNA template was removed by DNase I digestion. A total of 25 µl of the transcription mixture was mixed with 3 µl of 10× reaction buffer for DNase I (10 mM Tris-HCl pH 7.6 at 25 °C, 2.5 mM $MgCl_2$ and 0.5 mM $CaCl_2$, supplied with the enzyme) and 4 U of DNase I (NEB) and incubated at 37 °C for 60 min. The enzyme was heat-deactivated at 75 °C for 10 min and then immediately cooled on ice. All samples were purified using size-exclusion columns (Micro Bio-Spin P-6 gel columns, Biorad).

RNA 5′-polyphosphatase treatment of uncapped RNA transcripts

To obtain monophosphate RNA, uncapped RNA was treated with 20 U of 5′-polyphosphatase (Lucigen) in a solution of 1× buffer (supplied with the enzyme) in a total volume of 25 µl for 1 h at 37 °C. Samples were purified using size-exclusion columns (Micro Bio-Spin P-6 gel columns, Biorad).

Radiolabeling of RNA markers

The RNA markers having a sequence complementary to that of template TC and template CT (starting at the −1 and +1 position) and gTT (starting at the +1 position) were purchased from Eurofins genomics. The radiolabeling was performed in a volume of 20 µl using 0.6 µl of T4 polynucleotide kinase (NEB), 2 µl of T4 polynucleotide kinase reaction buffer (70 mM Tris-HCl pH 7.6 at 25 °C, 10 mM $MgCl_2$ and 5 mM DTT, supplied with the enzyme), 4.55 µl α-[^{32}P]ATP (activity: 9.25 MBq in 25 µl) and 0.75 µM RNA. The reaction mixture was incubated at 30 °C for 30 min and the enzyme was heat-deactivated at 65 °C for 20 min. The samples were purified using size-exclusion columns (Micro Bio-Spin P-6 gel columns, Biorad).

PAGE analysis of in vitro transcripts

Samples (10 µl) were mixed with 10 µl of 2× RNA loading dye (NEB), incubated at 75 °C for 5 min and then cooled on ice. Samples were loaded onto 12.5% polyacrylamide gels (with or without the addition of acryloylaminophenyl boronic acid (APB)) and electrophoretic separation was performed under denaturing conditions at 600 V for 3 h using 1× TBE as a running buffer. Denaturing PAGE gels were visualized by a Typhoon FLA 9500 imaging system and analyzed with ImageJ 1.53e software.

IVT for LC–MS analysis

IVT was performed in a volume of 25 µl containing 2 µM template DNA (Supplementary Table 1), 0.6 mM ATP, 0.6 mM GTP, 0.6 mM CTP, 1.6 mM Np_nNs, 5 mM Tris-HCl pH 7.9, 10 mM KCl, 1 mM $MgCl_2$, 0.1 mM DTT and 96 nM *Tt* RNAP. The mixture was incubated for 2 h at 65 °C. All samples were purified using MWCO filters (Sartorius, Vivacon 500, 10-kDa MWCO HY). The filters were prewashed once with 50 µl of the reaction buffer and then the samples diluted with 20 µl of molecular-biology-grade water were added and centrifuged at 13,000*g* for 15 min at room temperature. Samples were then analyzed by hydrophilic interaction liquid chromatography (HILIC) with MS detection.

LC–MS analysis of IVT products

RNA products were diluted tenfold with 50 mM ammonium acetate (pH 7.0). For the analysis, a high-performance LC instrument (Acquity H-class, Waters) equipped with an Xbridge Premier BEH amide column (2.5 µm and 4.6 mm × 150 mm; Waters) was used. The column temperature was 35 °C. Mobile phase A contained 20 mM ammonium acetate (Fisher) in a 90:10 v/v mixture of acetonitrile (Optima, Fisher) with ultrapure water (18.2 MΩ cm; Purelab Chorus system, Elga). Mobile phase B contained 20 mM ammonium acetate in ultrapure water. The autosampler was kept at 10 °C. The injection volume was 5 µl. The gradient of separation is shown in Supplementary Table 9. MS detection was performed on a Xevo G2-XS quadrupole time-of-flight (Q-TOF) MS instrument (Waters) equipped with an electrospray ionization source with parameters detailed in Supplementary Table 10. Fragmentation spectra of mass selected ions were generated with increased collision energy (30 eV). LC–MS data were acquired and analyzed with MassLynx version 4.2 software and graphs were prepared with GraphPad Prism 10.

TC plasmid preparation

The plasmid pRLG7558 containing p770 promoter driving the *veg* RNA expression and ribosomal RNA B (*rrnB*) under the P1 promoter[36] was a gift from the L. Krasny laboratory. In this plasmid, we substituted the *veg* promoter with our TC promoter sequence below using the EcoRI and HindIII restriction sites. The inserts were generated by annealing the following 5′-monophosphorylated oligonucleotides: forward: (5′-AATTCTCTTGACATAATCCATATGGTTGGGTATAATGGGAG**AG**-3′); reverse: (5′-AGCT**CT**CTCCCATTATACCCAACCATATGGATTATGTCAAGAG-3′)

The −1 and +1 positions in both strands are in bold.

The resulting constructs were verified by DNA sequencing. Plasmid DNA was purified using the PureLink HiPure plasmid midiprep kit (ThermoFisher Scientific), further extracted using phenol–chloroform purification and dissolved in pure water.

IVT with the TC plasmid

IVT was performed in a reaction volume of 25 µl containing 10 ng μl^{-1} TC plasmid (Supplementary Table 1), 1.6 mM Np_nNs (Ap_3A, Ap_4A, Ap_3G, Ap_4G, Gp_3G and Gp_4G; Jena Bioscience) and 1 µl of RNase Inhibitor (NEB), in the presence of reaction buffer containing 50 mM Tris-HCl (pH 7.9), 100 mM KCl, 10 mM $MgCl_2$, 1 mM DTT, 5 µg ml^{-1} BSA and 5% (v/v) glycerol. For reactions with *Tt* RNAP, 0.15 µM σ^A subunit and 0.05 µM *Tt* RNAP were added. For the reaction with *E. coli* RNAP, the supplied 1× reaction buffer (NEB) and 1 µl of *E. coli* RNAP holoenzyme (NEB) were used instead. A separated nucleotide mixture was prepared containing 0.6 mM ATP, 0.6 mM GTP, 0.6 mM UTP, 0.4 mM CTP and 0.3 µl of α-[^{32}P] CTP (activity: 9.25 MBq in 25 µl). Reaction mixtures without NTPs were preincubated for 10 min at 65 °C (*Tt* RNAP) or at 37 °C (*E. coli* RNAP), followed by addition of the NTP mix. Complete IVT reactions were then incubated for 2 h at 65 °C (*Tt* RNAP) or at 37 °C (*E. coli* RNAP). In negative control reactions, Np_nNs were replaced with GTP to observe only the +1 starting uncapped RNA. Following incubation, the samples were purified using size-exclusion columns (Micro Bio-Spin P-6 gel columns, Biorad).

PAGE analysis of IVT products from the TC plasmid

Samples (10 µl) were mixed with 10 µl of 2× RNA loading dye (NEB) and incubated at 90 °C for 5 min and then cooled on ice. Samples were loaded onto 8% polyacrylamide gels (with the addition of APB) and electrophoretic separation was performed under denaturing conditions at 600 V for 4 h using 1× TBE as a running buffer. Denaturing PAGE gels were visualized by a Typhoon FLA 9500 imaging system.

IVT with the TC plasmid for LC–MS analysis

IVT was performed as described above, with modified enzyme concentrations. Specifically, 0.3 µM σ^A subunit and 0.1 µM *Tt* RNAP were used in each 25-µl reaction. Following incubation, RNA samples were purified using RNA mini Quick Spin columns (Merck), eluting in 15 µl before LC–MS analysis.

Digestion of IVT products from the TC plasmid by RNase A

The RNA samples (15 µl) were mixed with 2.5 µl of ammonium acetate (500 mM, pH 7.5), 2.5 µl of EDTA (1 mM) and 5 µl of RNase A (200 ng μl^{-1}, NEB). RNase A specifically degrades single-stranded RNA after C and U residues leaving a phosphate at the 3′ end. The reaction was kept for 30 min at 37 °C. Right after, the reaction was transferred to an HPLC vial and directly measured by ion-pairing reverse-phase chromatography with MS detection.

LC–MS analysis of IVT products from the TC plasmid

Digested RNA products were separated on Acquity I-class (Waters) equipped with Acquity Premier oligonucleotide BEH C18 column (1.7 µm, 2.1 mm × 50 mm; Waters). The column temperature was 35 °C. Mobile phase A contained 15 mM triethylamine (Fisher) and 400 mM 1,1,1,3,3,3-hexafluoro-2-propanol (HFIP) in ultrapure water (18.2 MΩ cm; Purelab Chorus system, Elga). Mobile phase B contained 15 mM triethylamine and 400 mM HFIP in methanol (Optima, Fisher). The autosampler was kept at 10 °C. The injection volume was 10 µl. The gradient of separation is shown in Supplementary Table 11. MS detection was performed with the same Xevo G2-XS Q-TOF MS instrument. Ionization parameters are detailed in Supplementary Table 12.

Ap_4G purification for the cryo-EM study

To prevent contamination of the Ap_4G standard by pppApG, we treated Ap_4G and pppApG standard (used as a control, Jena Bioscience) with 1 U of nuclease P1 (NEB) in 1× buffer (50 mM ammonium acetate, pH 5.3) for 30 min at 37 °C followed by treatment with 0.03 U of shrimp alkaline phosphatase (NEB) in 1× rCutSmart buffer (50 mM potassium acetate, 20 mM Tris acetate, 10 mM magnesium acetate and 100 µg ml^{-1} recombinant albumin, pH 7.9 at 25 °C) and incubated for 10 min at 37 °C. The samples were purified using MWCO filters (Sartorius, Vivacon 500, 10-kDa MWCO HY). The filters were washed once with 50 µl of the reaction buffer and then samples, diluted with 20 µl of molecular-biology-grade water, were added and centrifuged at 10,000*g* for 10 min at room temperature. The samples were dried on a Speedvac system and dissolved in 50 µl of 50 mM ammonium acetate, pH 7.0. The filtrate was analyzed by LC–MS using the same method described above.

Cryo-EM grid preparation

In vitro reconstitution was performed in 30 µl of 50 mM Tris-HCl pH 7.9, 100 mM KCl, 10 mM $MgCl_2$, 1 mM DTT, 2.6 µM DNA template, 3.3 mM GTP or 1.6 mM Np_nNs, 1.6 mM CMPcPP or GMPcPP (Jena Bioscience), 1.3 µM *Tt* RNAP σ^A holoenzyme and an additional 1.5 µM σ^A. Each sample was incubated for ~10 min at 4 °C. Sample aliquots of 3 µl were applied to glow-discharged Quantifoil R2/1 Au 300-mesh grids, immediately blotted for 2 s and plunged into liquid ethane using a Thermo Fisher Scientific Vitrobot Mark IV (4 °C, 100% humidity).

Cryo-EM data collection

The grids were loaded into a 300-kV Titan Krios (FEI) electron microscope equipped with a Gatan K3 (model 1025) direct electron detector mounted on a Gatan BioQuantum (model 1967) energy filter. Data were collected using Serial EM software[44] in image shift acquisition mode (3 × 3 holes; 7–8 exposures per hole) at a nominal magnification of ×105,000 with a pixel size of 0.8336 Å per pixel. Videos were collected for 2–2.7 s at a flux of 15–20 electrons per $Å^2$ per s, giving a total exposure of around 40–50 electrons per $Å^2$. The defocus values ranged from −0.5 to −3.0 µm. In total, 40 frames of each video were saved, except aTT-Ap_4A, for which 46 frames were saved.

Cryo-EM image processing

All data processing (Supplementary Figs. 5 and 6 and Supplementary Tables 7 and 8) was performed using the RELION 4.0 software package[45]. Motion correction was performed using the RELION implementation of MotionCor2 (ref. 46). Videos were aligned using 7 × 5 patches with dose weighting. Contrast transfer function (CTF) was estimated using CTFFIND4.1 (ref. 47) from summed power spectra[48] for every four electrons per $Å^2$. From each dataset, 25 micrographs were randomly selected and a representative set of particles was picked manually. These particles, along with their coordinates, were pooled for the training of a consensus Topaz picking model[49]. Particles were subsequently picked from individual datasets by Topaz using this consensus-trained model.

After initial binning, particles underwent three rounds of two-dimensional classification. In each round, the particles were sorted into 200 classes with an *E*-step of 8 Å and a mask diameter of 240 Å. Only classes with well-defined structural features were retained and subjected to three-dimensional (3D) classification using a reference from the *Tt* RNAP crystal structure (PDB 4Q4Z)[37]. The first 3D classification sorted particles into ten classes with the regularization parameter set to $T = 4$ and an *E*-step of 5 Å. Quantitative analysis of the individual class types is summarized in Supplementary Table 8. Selected classes were aligned into a global 3D refinement. A subsequent 3D classification, using the result of the previous 3D refinement as input along with the corresponding mask, was performed using local searches from 3.7° to 1.8° with the regularization parameter increased to $T = 8$. Particles with poorly defined structural features were removed and the remaining particles were reextracted to native pixel size. Particles were refined globally again and corrected for aberrations, Bayesian-polished and 3D refined. The result of the refinement was used as input for focused 3D classification with masks around the broad core of the RNAP, performed at a local search interval of 0.5°, and the regularization parameter was increased to $T = 200$. Particles with poorly defined structural features for bound DNA were removed and the remaining particles were pooled and 3D refined. For TC-Ap_4G and aTT-Ap_4A, another round of focused 3D classification with masks around the RNAP AS was performed without angular searches. Classes were selected on the basis of features of the RNAP AS and pooled for the final 3D refinement. The final cryo-EM density maps were generated by the postprocessing feature in RELION and sharpened or blurred into MTZ format using CCP-EM[50]. The final set consisted of sharpened or blurred MTZ maps with $B = -200, -100, -50, 0, 50, 100$ and 200 $Å^2$. The resolution of the cryo-EM density maps (Supplementary Table 7 and Supplementary Fig. 6d) was estimated with the gold-standard Fourier shell correlation cutoff value of 0.143. Reference-based local amplitude scaling was performed by LocScale[51]. The angular orientation distribution of the 3D reconstruction was calculated by cryoEF (version 1.1.0)[52]. Local resolution was calculated within RELION 4.0.

Cryo-EM model building and refinement

The TC-Ap_3G model was built as follows. The X-ray structure of the *Tt* RNAP transcription initiation complex (PDB 4Q4Z)[37] was used as a starting model and docked into the cryo-EM map by Molrep[53]. The model was rebuilt manually in Coot (version 0.9.8.92)[54] against a blurred MTZ map ($B = 50$ $Å^2$) generated in CCP-EM[55]. Model self-restraints were used, as well as base pairing and parallelity restraints for DNA, Ap_3G and CMPcPP, which were automatically generated by the program libG[56] running under Refmac (version 5.8.0405)[57] within the CCP4 Interface (version 8.0.010)[58] and curated manually. The model was refined in real space[59] against a postprocessed MRC map in PHENIX (version 1.21-5207)[60], using self-restraints with the strict rotamer matching option enabled, as well as secondary-structure restraints, including base pairing and parallelity restraints for DNA, Ap_3G and CMPcPP. The restraints were generated automatically in PHENIX (version 1.21-5207)[60] and edited manually. In general, parallelity was maintained among adjacent bases of the Np_nNs, the extending nucleotide analogs and the nonpairing template base adjacent to the distal pairing Np_nN base. Distances and weights for the base-pairing hydrogen bonds were inferred from values used by libG[56] for canonical DNA base pairing. Ligand geometry restraints for Np_nNs and nucleotide analogs were generated using the Grade web server (version 2.0.14; Global Phasing). The final refinement round in PHENIX included one cycle of ADP refinement only. The refined models were validated using MolProbity[61] and the wwPDB database[62] validation server. The final TC-Ap_3G model was used as the starting model for the TC-GTP, TC-Ap_4G, TC-Ap_4A and aTT-Ap_4A models, which were built and refined analogously to the above description. In the case of TC-GTP, parallelity was also maintained between the GTP base and the adjacent nonpairing template base. The TC-empty structure was built and refined analogously, using the TC-Ap_4A template-shifted structure as the starting model.

Because of disorder, residues β′/217–339 from the β′ nonconserved domain were not included in any of the models. Additionally, residues σ/346–414, template-strand nucleotides 37–51 and nontemplate-strand nucleotides 3–17 were excluded from the TC-GTP, TC-Ap_4G, TC-Ap_4A, aTT-Ap_4A and TC-empty models.

The CMPcPP molecule in the TC-Ap_3G, TC-GTP, TC-Ap_4G and aTT-Ap_4A models was present in two conformations, one coordinating a magnesium cation (Mg^B) and one free of magnesium. The magnesium-coordinated conformation of CMPcPP was accompanied by a nearly closed conformation of the trigger loop, whereas the magnesium-free conformation of CMPcPP was associated with an alternative, unstructured conformation of the trigger loop. We describe the Mg^B-coordinated conformation with a nearly closed trigger loop in the Results. The TC-Ap_4A model, in which the template is antiscrunched by one nucleotide, comprises a GMPcPP in a single, Mg^B-coordinated conformation and the trigger loop is unstructured. In the TC-empty structure, the trigger loop is unstructured.

Reporting summary

Further information on research design is available in the Nature Portfolio Reporting Summary linked to this article.

Data availability

LC–MS data are available from Zenodo (https://doi.org/10.5281/zenodo.14215049)[63]. Coordinates and maps for *Tt* RNAP de novo transcription initiation complexes were deposited to the Protein Data Bank (PDB) and Electron Microscopy Data Bank (EMDB) under the following accession numbers: TC-Ap_3G, PDB 9FOG and EMD-50622;

TC-Ap$_4$G, PDB 9FOK and EMD-50625; TC-Ap$_4$A, PDB 9FP3 and EMD-50634; TC-GTP, PDB 9FO6 and EMD-50618; aTT-Ap$_4$A, PDB 9FRJ and EMD-50715; TC-empty, PDB 9R75 and EMD-53711. Source data are provided with this paper.

References

43. Stols, L. et al. A new vector for high-throughput, ligation-independent cloning encoding a tobacco etch virus protease cleavage site. *Protein Expr. Purif.* **25**, 8–15 (2002).
44. Mastronarde, D. N. Automated electron microscope tomography using robust prediction of specimen movements. *J. Struct. Biol.* **152**, 36–51 (2005).
45. Kimanius, D., Dong, L., Sharov, G., Nakane, T. & Scheres, S. H. W. New tools for automated cryo-EM single-particle analysis in RELION-4.0. *Biochem. J.* **478**, 4169–4185 (2021).
46. Zheng, S. Q. et al. MotionCor2: anisotropic correction of beam-induced motion for improved cryo-electron microscopy. *Nat. Methods* **14**, 331–332 (2017).
47. Rohou, A. & Grigorieff, N. CTFFIND4: fast and accurate defocus estimation from electron micrographs. *J. Struct. Biol.* **192**, 216–221 (2015).
48. McMullan, G., Vinothkumar, K. R. & Henderson, R. Thon rings from amorphous ice and implications of beam-induced Brownian motion in single particle electron cryo-microscopy. *Ultramicroscopy* **158**, 26–32 (2015).
49. Bepler, T. et al. Positive-unlabeled convolutional neural networks for particle picking in cryo-electron micrographs. *Res. Comput. Mol. Biol.* **10812**, 245–247 (2018).
50. Burnley, T., Palmer, C. M. & Winn, M. Recent developments in the CCP-EM software suite. *Acta Crystallogr. D* **73**, 469–477 (2017).
51. Jakobi, A. J., Wilmanns, M. & Sachse, C. Model-based local density sharpening of cryo-EM maps. *eLife* **6**, e27131 (2017).
52. Naydenova, K. & Russo, C. J. Measuring the effects of particle orientation to improve the efficiency of electron cryomicroscopy. *Nat. Commun.* **8**, 629 (2017).
53. Vagin, A. & Teplyakov, A. Molecular replacement with MOLREP. *Acta Crystallogr. D* **66**, 22–25 (2010).
54. Emsley, P. & Cowtan, K. Coot: model-building tools for molecular graphics. *Acta Crystallogr. D* **60**, 2126–2132 (2004).
55. Wood, C. et al. Collaborative computational project for electron cryo-microscopy. *Acta Crystallogr. D* **71**, 123–126 (2015).
56. Brown, A. et al. Tools for macromolecular model building and refinement into electron cryo-microscopy reconstructions. *Acta Crystallogr. D* **71**, 136–153 (2015).
57. Kovalevskiy, O., Nicholls, R. A., Long, F., Carlon, A. & Murshudov, G. N. Overview of refinement procedures within REFMAC5: utilizing data from different sources. *Acta Crystallogr. D* **74**, 215–227 (2018).
58. Winn, M. D. et al. Overview of the CCP4 suite and current developments. *Acta Crystallogr. D* **67**, 235–242 (2011).
59. Afonine, P. V. et al. Real-space refinement in PHENIX for cryo-EM and crystallography. *Acta Crystallogr. D* **74**, 531–544 (2018).
60. Liebschner, D. et al. Macromolecular structure determination using X-rays, neutrons and electrons: recent developments in PHENIX. *Acta Crystallogr. D* **75**, 861–877 (2019).
61. Williams, C. J. et al. MolProbity: more and better reference data for improved all-atom structure validation. *Protein Sci.* **27**, 293–315 (2018).
62. Berman, H., Henrick, K. & Nakamura, H. Announcing the worldwide Protein Data Bank. *Nat. Struct. Biol.* **10**, 980 (2003).
63. Molecular insight into 5′ RNA capping with dinucleoside polyphosphates by bacterial RNA polymerase. *Zenodo* https://doi.org/10.5281/zenodo.14215049 (2025).

Acknowledgements

We are grateful to all members of the H.C. group for their help and advice; to L. Gahurová for help with the design of the template; and to M. Lepšík, H. Martinez-Seara Monne and K. K. Telukunta from the High-Performance Computing Core Facility of the Institute of Organic Chemistry and Biochemistry of the Czech Academy of Sciences (IOCB Prague) for support. We thank M. Klíma and P. Pachl from IOCB Prague for advice on the definition of restraints. We thank the staff of the CEITEC facility, especially J. Nováček and Z. Hlavenková, for access to the Krios microscope and the Czech Infrastructure for Integrative Structural Biology (CIISB) Instruct-CZ Center, supported by the Ministry of Education, Youth and Sports of the Czech Republic (LM2023042), the European Regional Development Fund-Project 'UP CIISB' (no. CZ.02.1.01/0.0/0.0/18_046/0015974) and the European Regional Development Fund-Project 'Innovation of Czech Infrastructure for Integrative Structural Biology' (no. CZ.02.01.01/00/23_015/0008175). We acknowledge funding from the European Research Council Executive Agency under the European Union's Horizon Europe Framework Program for Research and Innovation (grant no. 101041374, StressRNaction, to H.C.) and the Operational Program Johannes Amos Comenius project 'RNA for Therapy' (CZ.02.01.01/00/22_008/0004575, to H.C. and P.Ř.), cofinanced by the EU. The schematic in the graphical abstract (online) was created in BioRender. Serianni, V. (2025) https://BioRender.com/qdn74rj.

Author contributions

H.C., T.K. and P.Ř. conceptualized and supervised the project. V.M.S., A.Š., T.K. and H.C. designed the experiments. M.F. carried out the cloning. T.V. expressed and purified proteins for biochemistry experiments and cryo-EM. V.M.S. performed the transcription experiments and prepared cryo-EM samples. A.Š. carried out the LC–MS analyses. A.F. prepared the cryo-EM grids. A.F. and T.K. collected the cryo-EM data. A.K.D. and H.Š. performed the cryo-EM image processing and 3D reconstruction. J.Š. built the initial models together with H.Š. and T.K. J.Š. refined the final atomic models. H.C., T.K., V.M.S. and J.Š. wrote the manuscript with input from all coauthors. V.M.S., T.K., J.Š., A.K.D. and H.Š. prepared the figures. All authors discussed the manuscript and contributed to the interpretation of the data.

Competing interests

The authors declare no competing interests.

Additional information

Extended data is available for this paper at https://doi.org/10.1038/s41589-025-02134-5.

Supplementary information The online version contains supplementary material available at https://doi.org/10.1038/s41589-025-02134-5.

Correspondence and requests for materials should be addressed to Tomáš Kouba or Hana Cahova.

Peer review information *Nature Chemical Biology* thanks Richard Ebright and the other, anonymous, reviewer(s) for their contribution to the peer review of this work.

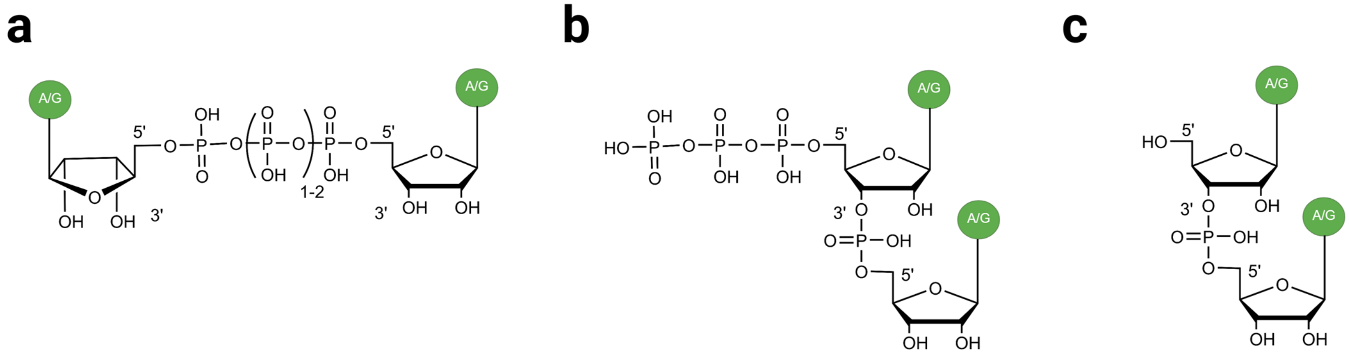

Extended Data Fig. 1 | Distinct phosphodiester linkages in Np$_n$Ns and canonical RNA. Chemical structures of Np$_n$Ns (**a**), pppNpN nascent RNA dinucleotide (**b**) and NpN 5′-end hydroxyl dinucleotide primer (**c**). Created in BioRender. Serianni, V. (2025) https://BioRender.com/qasouxb.

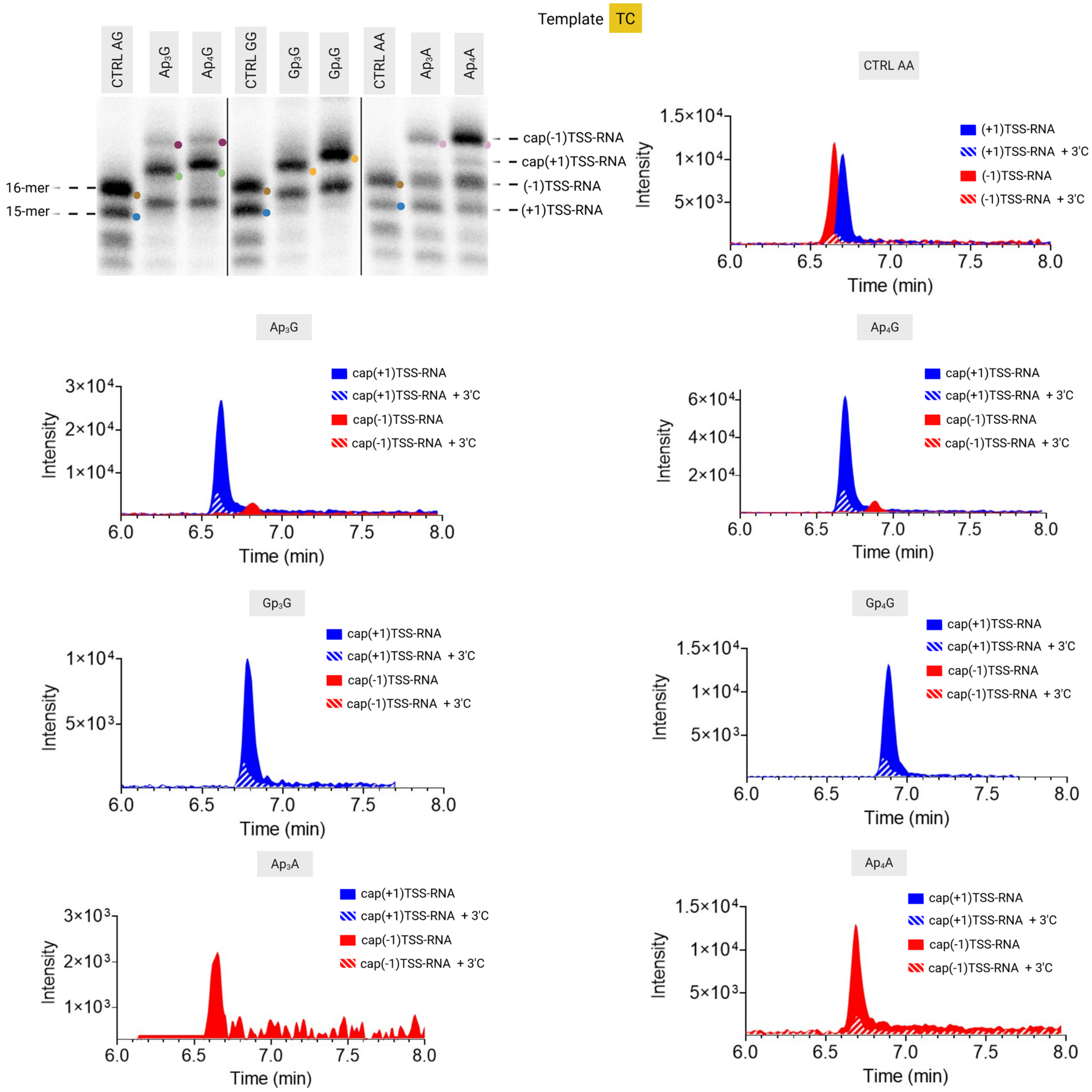

Extended Data Fig. 2 | LC-MS analysis of IVT products with template TC. Extracted ion chromatograms of IVT products with and without addition of $\mathrm{Np}_n\mathrm{Ns}$. IVT products encoded from the +1 TSS are marked blue, IVT products encoded from the +1 TSS with an extra C added at the 3′ end are marked dashed blue. IVT products encoded from the −1 TSS are marked red, IVT products encoded from the −1 TSS with an extra C added at the 3′ end are marked dashed red. The sequences of the formed products with exact masses are shown in Supplementary Table 3. The PAGE gel from Fig. 1d is reproduced here for clarity (see Fig. 1c-e legend). Created in BioRender. Serianni, V. (2025) https://BioRender.com/55wowug.

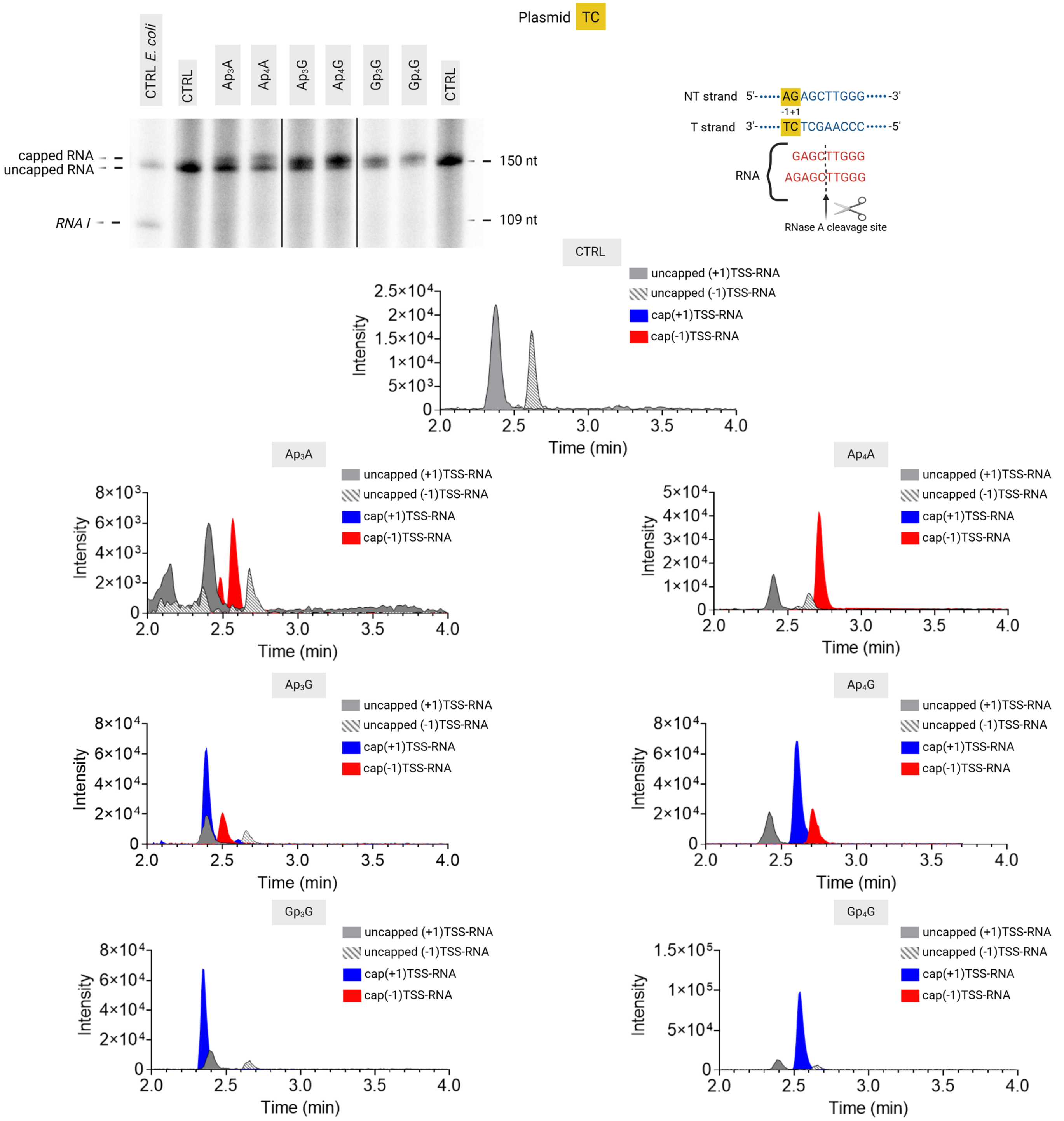

Extended Data Fig. 3 | PAGE analysis and LC-MS analysis of IVT products generated from plasmid TC. PAGE analysis (with APB) shows RNA products obtained from IVT reactions using the TC plasmid and NTPs or their combination with Np$_n$Ns radiolabeled with α-[^{32}P]CTP. The IVT reaction was performed in five independent experiments. The controls (CTRL *E. coli* and CTRL) show the migration of the uncapped RNA (150 nt) produced by *E. coli* RNAP and *Tt* RNAP, respectively, and serve as molecular weight markers. Moreover, the formation of the known RNAI encoded in the plasmid (109 nt) and produced by *E. coli* RNAP was observed. Non-radiolabeled RNA was used for digestion with RNase A (cleaving after pyrimidines) and further analyzed by LC-MS. Extracted ion chromatograms show RNA fragments generated from IVT with or without Np$_n$Ns. Uncapped RNA (CTRL) is indicated in gray: solid gray lines represent transcripts initiating at the +1 TSS (defined as uncapped(+1)TSS-RNA), while dashed gray lines represent transcripts initiating at the −1 TSS (defined as uncapped(−1) TSS-RNA). Capped IVT products encoded from the +1 TSS (cap(+1)TSS-RNA) are shown in blue and products encoded from the −1 TSS (cap(−1)TSS-RNA) are shown in red. The sequences and exact masses of the corresponding products are listed in Supplementary Table 4. Created in BioRender. Serianni, V. (2025) https://BioRender.com/pbscak2.

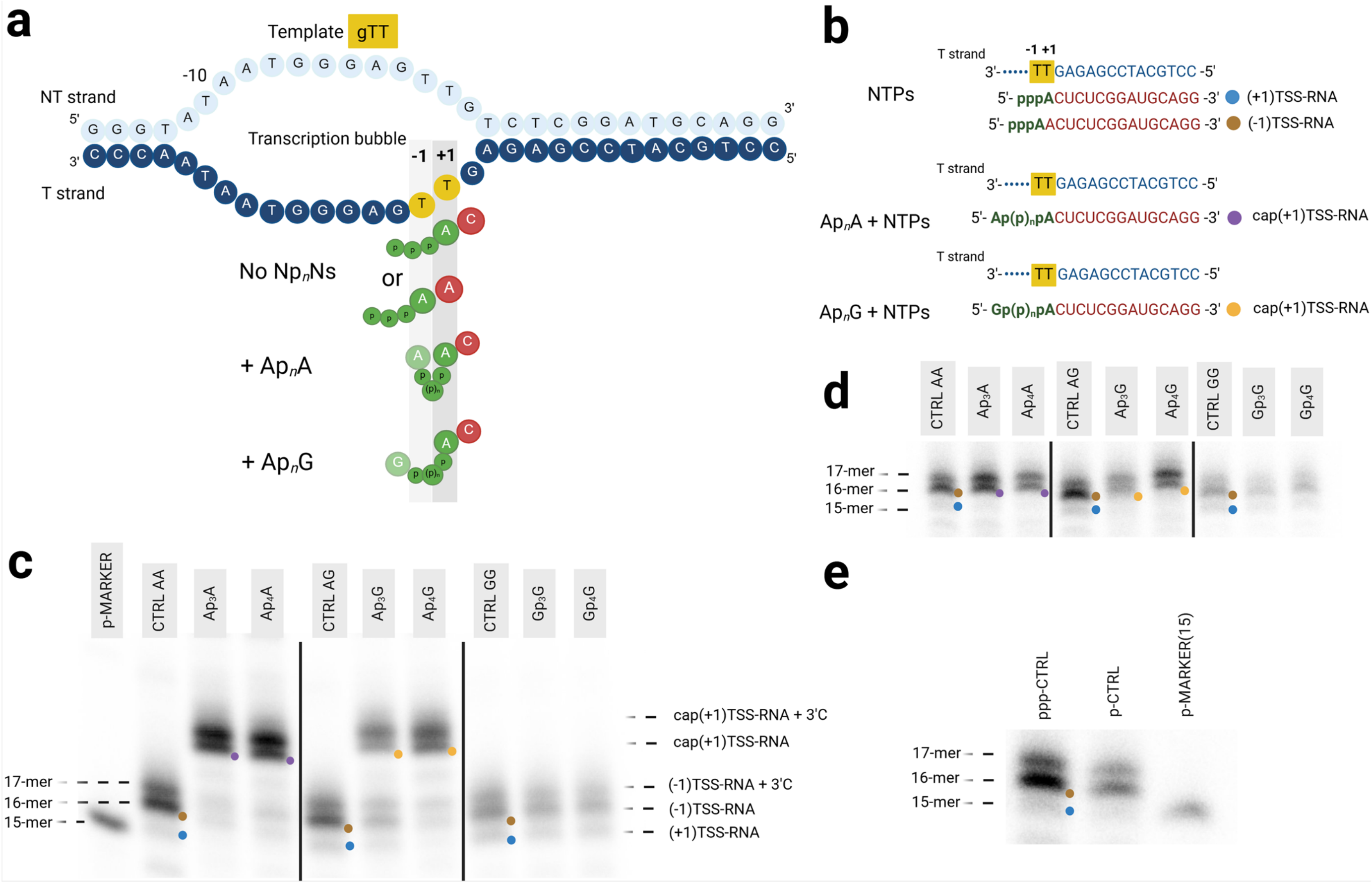

Extended Data Fig. 4 | IVT reactions with Np$_n$Ns and the template gTT. **a**, Schemes of IVT experiments showing NTPs or Np$_n$Ns binding to the template gTT (with a pre-melted bubble from position −11 to +2) during transcription initiation with different base pairing at the −1 and +1 positions. **b**, Sequences of color-coded RNA products with and without the addition of Np$_n$Ns. Uncapped 15-mer referred to as (+1)TSS-RNA is indicated by a blue dot, uncapped 16-mer referred to as (−1)TSS-RNA is indicated by a brown dot, capped 15-mers referred to as cap(+1)TSS-RNA are indicated by violet and yellow dots. **c**, PAGE (with APB) showing RNA products obtained from IVT reactions with the template gTT and NTPs or their combination with Np$_n$Ns radiolabeled with α-[^{32}P]CTP. Each control (CTRL AG, CTRL GG, CTRL AA), designed according to Supplementary Table 2, shows the migration of the uncapped RNA 15-mer and 16-mer and serves as a molecular weight marker (panel **e**). The capped products are marked with colored dots according to panel **b**. We observed also the formation of uncapped 17-mer with an extra C added at the 3′ end. The label '+ 3′C' indicates RNA transcripts with an extra 3′ C, as determined by LC-MS (see Extended Data Figure 5). The IVT was performed in ten independent experiments; one representative gel is shown. **d**, PAGE (without APB) was used to analyze RNA products obtained from IVT reactions. The reactions were performed as in panel **c** and it shows that, without APB, there is no difference in migration between capped and uncapped RNA. The controls/markers are analogous to panel **c**. **e**, PAGE (without APB) shows the migration of 15-mer monophosphate marker (p-MARKER(15)) along with the monophosphate RNA (p-CTRL) and triphosphate RNA (ppp-CTRL) generated using template gTT and regular NTPs. The experiment was performed in triplicate. Created in BioRender. Serianni, V. (2025) https://BioRender.com/fggd152.

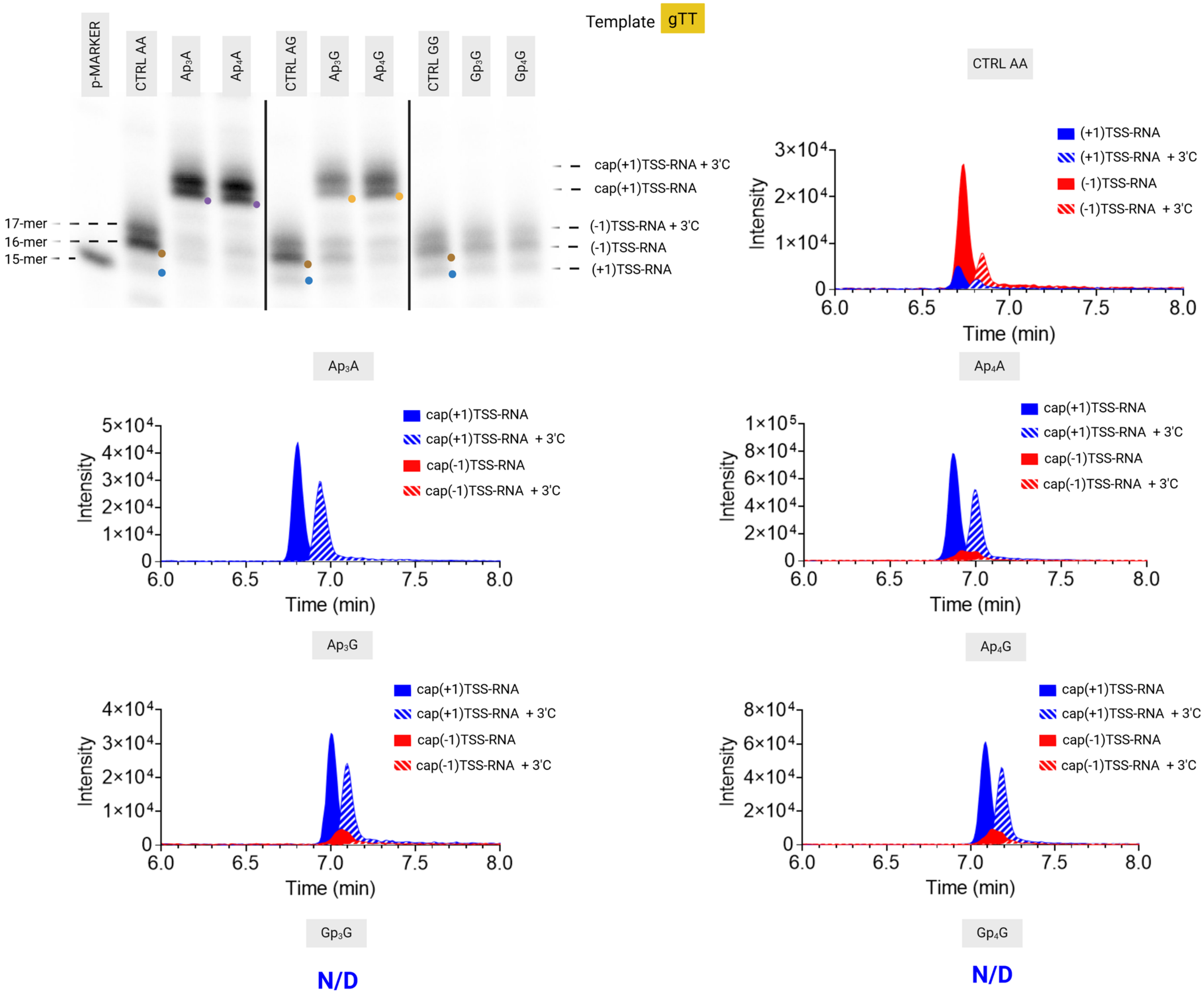

Extended Data Fig. 5 | LC-MS analysis of IVT products with template gTT. The PAGE gel from Extended Data Fig. 4c is reproduced here for clarity. Extracted ion chromatograms of IVT products with and without addition of Np$_n$Ns. IVT products encoded from the +1 TSS are marked blue, IVT products encoded from the +1 TSS with an extra C added at the 3′ end are marked dashed blue. IVT products encoded from the −1 TSS are marked red, IVT products encoded from the −1 TSS with an extra C added at the 3′ end are marked dashed red. The sequences of the formed products with exact masses are shown in Supplementary Table 5. We confirmed the 16-mer product encoded from the −1 TSS and we detected a 17-mer RNA product corresponding with its mass also to the (−1)TSS-RNA but with an extra C added at the 3′ end. Only trace amounts of the 15-mer RNA encoded from the +1 TSS were detected by PAGE and LC-MS. The PAGE analysis of IVT reactions with Ap$_{3\text{-}4}$A and the template gTT showed the formation of two capped products. LC-MS analysis confirmed the production of capped RNA encoded from the +1 TSS, but contrary to the control IVT, we did not detect capped RNA encoded from the −1 TSS. The second observed product has the mass of cap(+1)TSS-RNA with the 3′ extra C. These observations indicate that Ap$_{3\text{-}4}$A initiate transcription only from the +1 TSS of the gTT template. The experiment with Ap$_{3\text{-}4}$G led to the formation of similar products as in the case of Ap$_{3\text{-}4}$A. As expected, Gp$_{3\text{-}4}$G cannot base pair with the gTT template and did not produce capped RNA. N/D = not detected. Created in BioRender. Serianni, V. (2025) https://BioRender.com/jj7ixi3 .

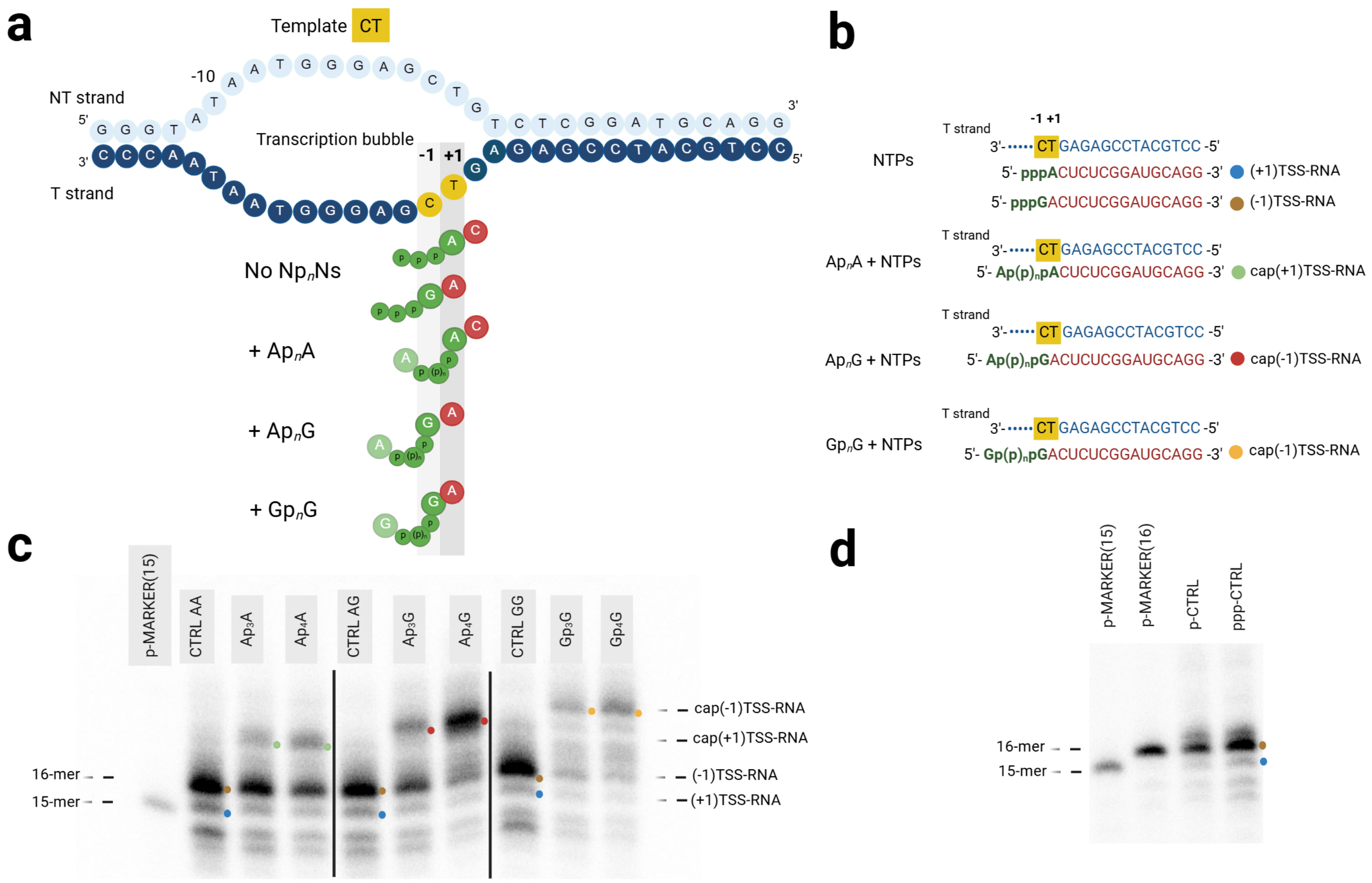

Extended Data Fig. 6 | IVT with Np$_n$Ns and template CT. a, Schemes of IVT experiments showing NTPs or Np$_n$Ns binding to the template CT (with a pre-melted bubble from position −11 to +2) during transcription initiation with different base pairing at the −1 and +1 positions. **b**, Sequences of color-coded RNA products with and without the addition of Np$_n$Ns. Uncapped 15-mer referred to as (+1)TSS-RNA is indicated by a blue dot, uncapped 16-mer referred to as (−1)TSS-RNA is indicated by a brown dot, capped 15-mer referred to as cap(+1)TSS-RNA is indicated by a green dot, and capped 16-mers referred to as cap(−1)TSS-RNA are indicated by red and yellow dots. **c**, PAGE (with APB) showing RNA products from IVT using the template CT with NTPs or various Np$_n$Ns, radiolabeled with α-[^{32}P] CTP. Each control (CTRL AG, CTRL GG, CTRL AA, Supplementary Table 2) shows the migration of the uncapped RNA 15-mer and 16-mer and serves as size marker (panel **d**). IVT reaction (Extended Data Table 1) without Np$_n$Ns led to the production of mainly 16-mer and also 15-mer uncapped products. The RNA products are marked according to panel **b**. We observed formation of capped 15-mer RNA encoded from the +1 T position when Ap$_{3\text{-}4}$A were added to IVT. When Ap$_{3\text{-}4}$G and Gp$_{3\text{-}4}$G were added, we observed mainly capped 16-mer RNA encoded from the −1 C position of the template. This indicates that the transcription was initiated by the G nucleoside of Gp$_n$Ns bound at the −1 C position of the template. The IVT was performed in ten independent experiments; one representative gel is shown. **d**, PAGE (without APB) shows migration of 15-mer (p-MARKER(15)) and 16-mer (p-MARKER(16)) monophosphate marker along with the monophosphate RNA (p-CTRL) and triphosphate RNA (ppp-CTRL) generated using template CT and regular NTPs. The experiment was performed in triplicate. Created in BioRender. Serianni, V. (2025) https://BioRender.com/opxr6fh .

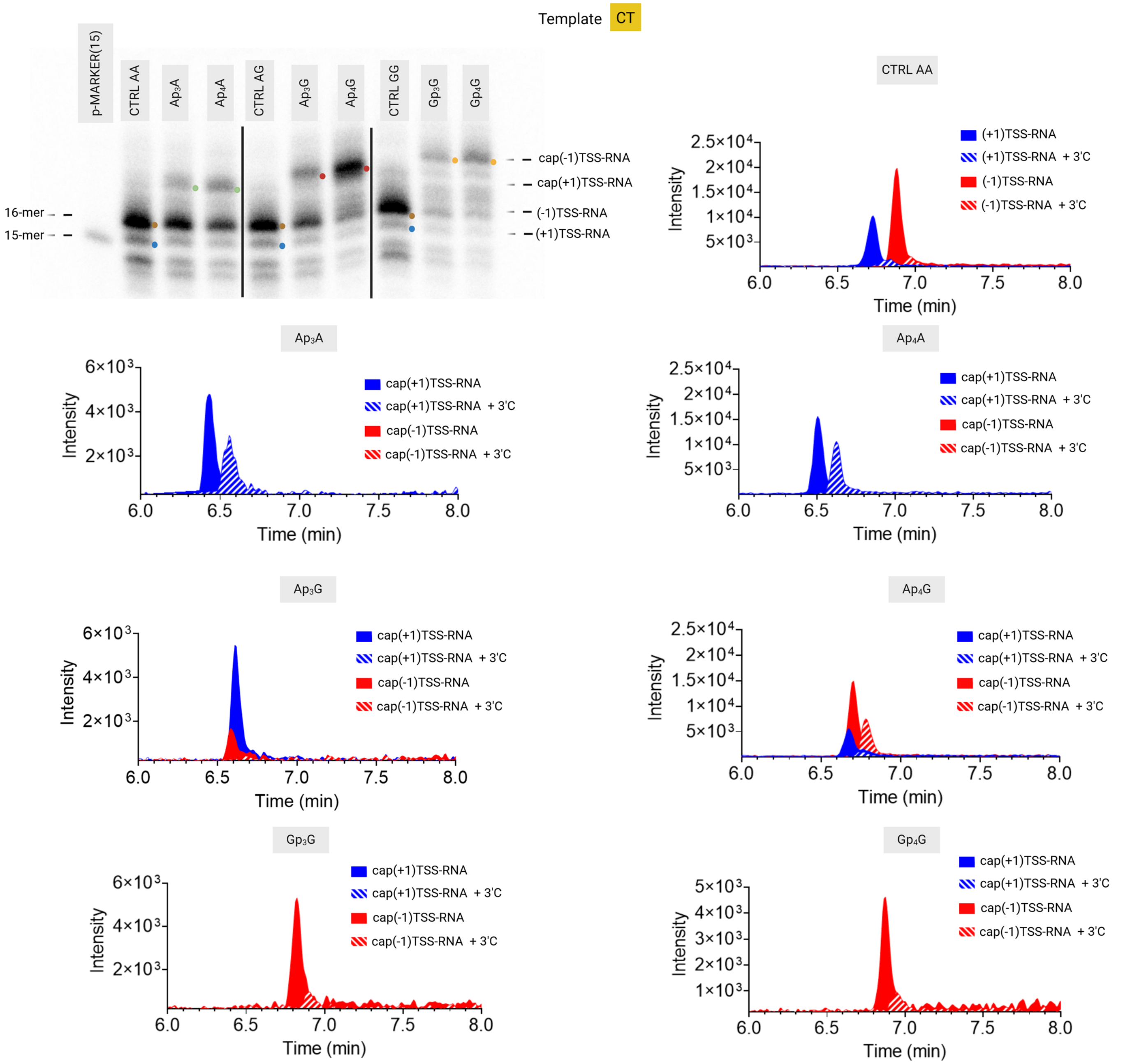

Extended Data Fig. 7 | LC-MS analysis of IVT products with template CT. The PAGE gel from Extended Data Fig. 6c is reproduced here for clarity. Extracted ion chromatograms of IVT products with and without addition of Np$_n$Ns. IVT products encoded from the +1 TSS are marked blue, IVT products encoded from the +1 TSS with an extra C added at the 3′ end are marked dashed blue. IVT products encoded from the −1 TSS are marked red, IVT products encoded from the −1 TSS with an extra C added at the 3′ end are marked dashed red. The sequences of the formed products with exact masses are shown in Supplementary Table 6. Majority of our observations from the PAGE analysis were also confirmed by the LC-MS analysis. The only exception was the reaction with Ap$_3$G, which led to the formation of capped RNA encoded from the +1 TSS as the main product. We also observed the formation of products with an extra C added at the 3′ end. Created in BioRender. Serianni, V. (2025) https://BioRender.com/xnjca7i .

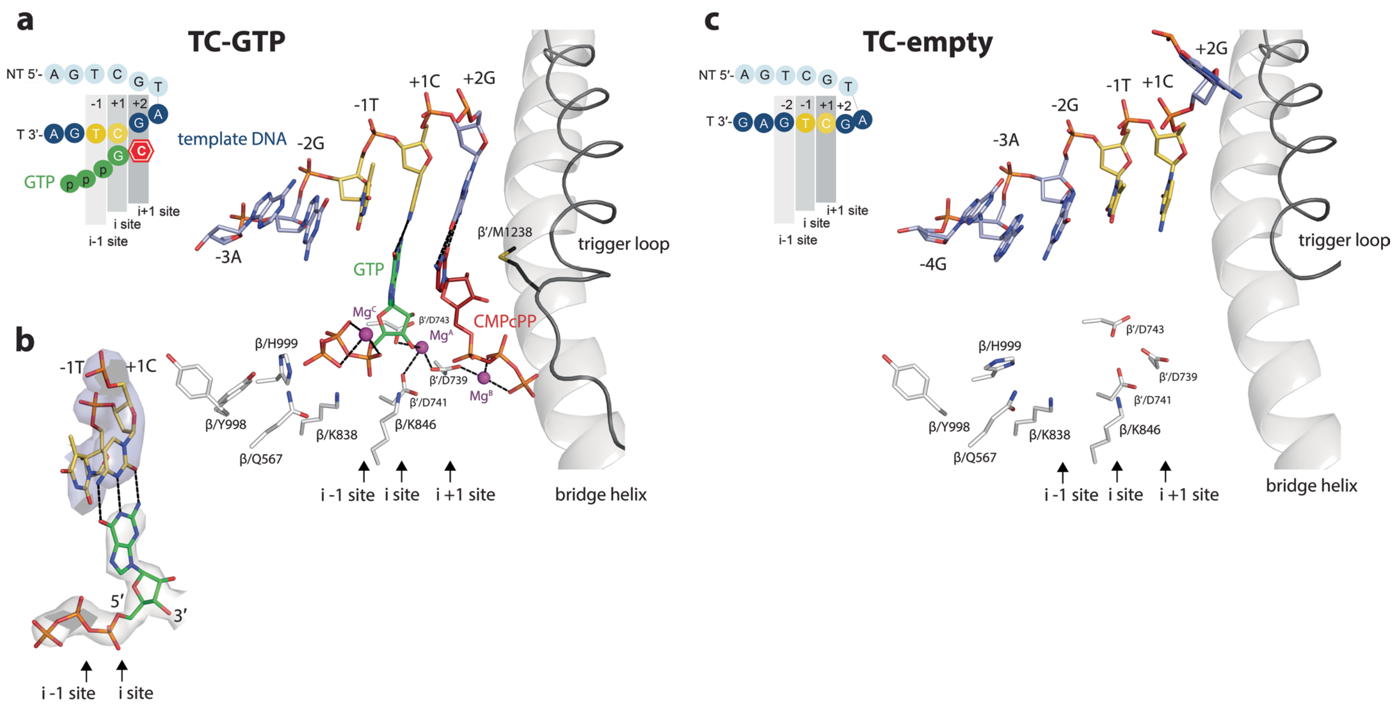

Extended Data Fig. 8 | GTP bound in de novo transcription initiation complex; anti-scrunched template strand in the TC-empty complex. **a**, AS structure of de novo transcription initiation, where GTP binds canonically in the *i* site and CMPcPP is bound in a pre-insertion position in the *i* + 1 site, consistent with the trigger loop being only partially closed towards the AS. The DNA template strand is marked with respect to the +1 TSS site. The aspartate triad of the AS coordinates Mg^A and partially also Mg^B. Conserved residues are positioning the GTP phosphates, which themselves coordinate an additional Mg^C ion. **b**, Cryo-EM density for the GTP in the *i* site (transparent gray), base pairing with the template +1 C (transparent blue). **c**, When the AS is unoccupied, the template strand is antiscrunched by one nucleotide in respect to when the AS is occupied by GTP and CMPcPP (panel **a**). The template −2 G base is in line with the *i* − 1 site, the template −1 T base is in line with the *i* site and the template +1 C base is in line with the *i* + 1 site. The +2 G base is shifted over the bridge helix towards the downstream DNA duplex.

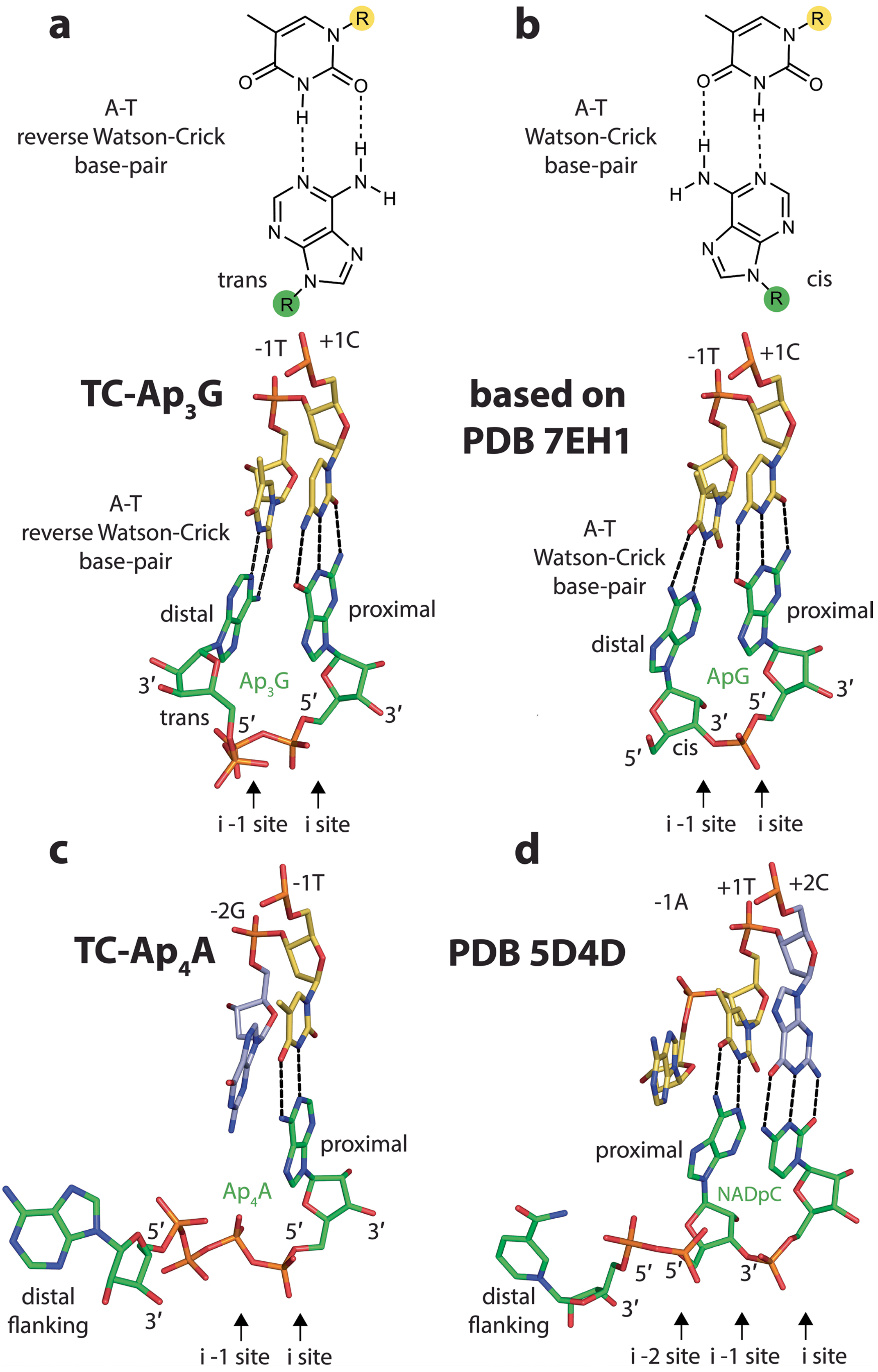

Extended Data Fig. 9 | See next page for caption.

Extended Data Fig. 9 | Comparison of WC and rWC base pairing, and NAD binding to RNAP AS. a, In TC-Ap$_3$G, the glycosidic bond of the distal Ap$_3$G adenosine and the glycosidic bond of the template −1 T are in mutual trans orientation, which results in their reverse WC base pairing. **b**, In a regular RNA/DNA duplex, here represented by a 5′-end hydroxyl dinucleotide primer/DNA complex (PDB 7EH1), the glycosidic bond of the distal adenosine in ApG (featuring regular 5′ to 3′ monophosphate linker) and the glycosidic bond of the template −1 T are in mutual cis orientation, which favors canonical WC base pairing. The original CC template and GpG dinucleotide in PDB ID 7EH1 were mutated to TC and ApG for the sake of direct comparison of A-T base pairing in the $i-1$ site. **c**, In TC-Ap$_4$A, the distal Ap$_4$A adenosine flanks due to purine-purine base-pairing incompatibility at the $i-1$ site. **d**, NAD as NCIN visualized after incorporation into nascent product and translocation (PDB 5D4D). The proximal adenosine of NAD base pairs in the $i-1$ site, while the distal nicotinamide moiety does not base pair with the template strand adenine purine base in line with the $i-2$ site. A direct comparation of NAD and Np$_4$N binding at the *i* and $i-1$ site of the AS during the very initial step of transcription awaits the determination of a structure with NAD bound in the respective sites.

Extended Data Table 1 | Sequences of template and non-template DNA strands used to construct artificial DNA promoters with pre-formed transcription bubbles

DNA name	Sequence
TC template	NT 5′-CTCTTGACATAATCCATATGGTTGGGTATAATGGGAGT**C**GTCTCGGATGCAGG-3′
	T 3′-GAGAACTGTATTAGGTATACCAACCCAATAATGGGAGT**C**GAGAGCCTACGTCC-5′
gTT template	NT 5′-CTCTTGACATAATCCATATGGTTGGGTATAATGGGAGT**T**GTCTCGGATGCAGG-3′
	T 3′-GAGAACTGTATTAGGTATACCAACCCAATAATGGGAGT**T**GAGAGCCTACGTCC-5′
CT template	NT 5′-CTCTTGACATAATCCATATGGTTGGGTATAATGGGAGC**T**GTCTCGGATGCAGG-3′
	T 3′-GAGAACTGTATTAGGTATACCAACCCAATAATGGGAGC**T**GAGAGCCTACGTCC-5′
aTT template	NT 5′-CTCTTGACATAATCCATATGGTTGGGTATAATGGGAT**T**GTCTCGGATGCAGG-3′
	T 3′-GAGAACTGTATTAGGTATACCAACCCAATAATGGGAT**T**GAGAGCCTACGTCC-5′
tTC template	NT 5′-CTCTTGACATAATCCATATGGTTGGGTATAATGGGAGT**C**GTCTCGGATGCAGG-3′
	T 3′-GAGAACTGTATTAGGTATACCAACCCAATAATGGGATT**C**GAGAGCCTACGTCC-5′
AT template	NT 5′-CTCTTGACATAATCCATATGGTTGGGTATAATGGGAGA**T**GTCTCGGATGCAGG-3′
	T 3′-GAGAACTGTATTAGGTATACCAACCCAATAATGGGAGA**T**GAGAGCCTACGTCC-5′

The sequences have various combinations of nucleotides at the −1 and +1 positions (indicated by capital letters in the template names while the −2 position is shown in lower-case). The aTT template is shortened by one nucleotide. NT strand = non-template strand 5′ to 3′; T = template strand 3′ to 5′. The +1 consensus transcription start sites are bold. DNA templates used for transcription and cryo-EM analyses were prepared by annealing NT and T strands with the same name, except for tTC (T strand, Supplementary Table 1), which was annealed with the TC (NT strand). Pre-formed transcription bubbles are underlined.

nature portfolio

Corresponding author(s):	Tomáš Kouba, Hana Cahova
Last updated by author(s):	Dec 8, 2025

Reporting Summary

Nature Portfolio wishes to improve the reproducibility of the work that we publish. This form provides structure for consistency and transparency in reporting. For further information on Nature Portfolio policies, see our Editorial Policies and the Editorial Policy Checklist.

Statistics

For all statistical analyses, confirm that the following items are present in the figure legend, table legend, main text, or Methods section.

n/a	Confirmed	
☐	☒	The exact sample size (*n*) for each experimental group/condition, given as a discrete number and unit of measurement
☐	☒	A statement on whether measurements were taken from distinct samples or whether the same sample was measured repeatedly
☒	☐	The statistical test(s) used AND whether they are one- or two-sided *Only common tests should be described solely by name; describe more complex techniques in the Methods section.*
☒	☐	A description of all covariates tested
☒	☐	A description of any assumptions or corrections, such as tests of normality and adjustment for multiple comparisons
☐	☒	A full description of the statistical parameters including central tendency (e.g. means) or other basic estimates (e.g. regression coefficient) AND variation (e.g. standard deviation) or associated estimates of uncertainty (e.g. confidence intervals)
☒	☐	For null hypothesis testing, the test statistic (e.g. *F*, *t*, *r*) with confidence intervals, effect sizes, degrees of freedom and *P* value noted *Give P values as exact values whenever suitable.*
☒	☐	For Bayesian analysis, information on the choice of priors and Markov chain Monte Carlo settings
☒	☐	For hierarchical and complex designs, identification of the appropriate level for tests and full reporting of outcomes
☒	☐	Estimates of effect sizes (e.g. Cohen's *d*, Pearson's *r*), indicating how they were calculated

Our web collection on statistics for biologists contains articles on many of the points above.

Software and code

Policy information about availability of computer code

Data collection	Titan Krios (FEI) + Serial EM 4.1, LC-MS: Acquity H-class + Xevo G2-XS QTof mass spectrometer (Waters), Typhoon FLA 9500
Data analysis	MotionCor2 v1.3.1, CTFFIND4.1, TOPAZ v0.2.5, RELION 4.0, CCP-EM 1.5, LocScale 0.1, cryoEF v1.1.0, Molprep 11.7.02, Coot 0.9.8.92, CCP4 Interface 8.0.010, libG under Refmac 5.8.0405, Phenix 1.21-5207, Grade Web Server 2.0.14, MolProbity Server 4.5.2, GraphPad Prism 10, MassLynx V4.2, ImageJ 1.53e

For manuscripts utilizing custom algorithms or software that are central to the research but not yet described in published literature, software must be made available to editors and reviewers. We strongly encourage code deposition in a community repository (e.g. GitHub). See the Nature Portfolio guidelines for submitting code & software for further information.

Data

Policy information about availability of data

All manuscripts must include a data availability statement. This statement should provide the following information, where applicable:

- Accession codes, unique identifiers, or web links for publicly available datasets
- A description of any restrictions on data availability
- For clinical datasets or third party data, please ensure that the statement adheres to our policy

All data generated in this study are available within the article and supplementary information. Source data are provided with this paper paper in Source data File. LC-MS data are available at 10.5281/zenodo.14215050. Co-ordinates and maps for Thermus thermophilus RNA polymerase de novo transcription initiation complexes have been deposited in the wwPDB and EMDB databases under the following accession numbers: TC-Ap3G - 9FOG and EMD-50622, TC-Ap4G - 9FOK and EMD-50625, TC-Ap4A - 9FP3 and EMD-50634, TC-GTP - 9FO6 and EMD-50618, aTT-Ap4A - 9FRJ and EMD-50715, TC-empty - 9R75 and EMD-53711.

Research involving human participants, their data, or biological material

Policy information about studies with human participants or human data. See also policy information about sex, gender (identity/presentation), and sexual orientation and race, ethnicity and racism.

Reporting on sex and gender	Not relevant, since no experiments on humans were performed in this study.
Reporting on race, ethnicity, or other socially relevant groupings	Not relevant, since no experiments on humans were performed in this study.
Population characteristics	Not relevant, since no experiments on humans were performed in this study.
Recruitment	Not relevant, since no experiments on humans were performed in this study.
Ethics oversight	Not relevant, since no experiments on humans were performed in this study.

Note that full information on the approval of the study protocol must also be provided in the manuscript.

Field-specific reporting

Please select the one below that is the best fit for your research. If you are not sure, read the appropriate sections before making your selection.

☒ Life sciences ☐ Behavioural & social sciences ☐ Ecological, evolutionary & environmental sciences

For a reference copy of the document with all sections, see nature.com/documents/nr-reporting-summary-flat.pdf

Life sciences study design

All studies must disclose on these points even when the disclosure is negative.

Sample size	For biochemical analyses, sample sizes of at least of 3 were chosen (experimental replicates).
Data exclusions	No data were excluded.
Replication	The number of times each experiment was replicated is indicated in the figure captions.
Randomization	not applicable
Blinding	not applicable

Reporting for specific materials, systems and methods

We require information from authors about some types of materials, experimental systems and methods used in many studies. Here, indicate whether each material, system or method listed is relevant to your study. If you are not sure if a list item applies to your research, read the appropriate section before selecting a response.

Materials & experimental systems

n/a	Involved in the study
☒	☐ Antibodies
☒	☐ Eukaryotic cell lines
☒	☐ Palaeontology and archaeology
☒	☐ Animals and other organisms
☒	☐ Clinical data
☒	☐ Dual use research of concern
☒	☐ Plants

Methods

n/a	Involved in the study
☒	☐ ChIP-seq
☒	☐ Flow cytometry
☒	☐ MRI-based neuroimaging

Plants

Seed stocks	Not relevant, as no experiments on plants were performed in this study
Novel plant genotypes	Not relevant, as no experiments on plants were performed in this study
Authentication	Not relevant, as no experiments on plants were performed in this study